

## Rapid Rotation of an Erupting Prominence and the Associated Coronal Mass Ejection on 13 May 2013

Yuhao Zhou<sup>1,2</sup> · Haisheng Ji<sup>1</sup> ·  
Qingmin Zhang<sup>1</sup>

© Springer

**Abstract** In this paper, we report the multiwavelength observations of an erupting prominence and the associated coronal mass ejection (CME) on 13 May 2013. The event occurs behind the western limb in the field of view of the Atmospheric Imaging Assembly (AIA) on board the Solar Dynamics Observatory (SDO) spacecraft. The prominence is supported by a highly twisted magnetic flux rope and shows rapid rotation in the counterclockwise direction during the rising motion. The rotation of the prominence lasts for  $\sim 47$  minutes. The average period, angular speed, and linear speed are  $\sim 806$  s,  $\sim 0.46$  rad  $\text{min}^{-1}$ , and  $\sim 355$  km  $\text{s}^{-1}$ , respectively. The total twist angle reaches  $\sim 7\pi$ , which is considerably larger than the threshold for kink instability. Writhing motion during 17:42–17:46 UT is clearly observed by SWAP in 174 Å and Extreme-Ultraviolet Imager (EUVI) on board the behind Solar Terrestrial Relations Observatory (STEREO) spacecraft in 304 Å after reaching an apparent height of  $\sim 405$  Mm. Therefore, the prominence eruption is most probably triggered by kink instability. A pair of conjugate flare ribbons and post-flare loops are created and observed by STA/EUVI. The onset time of writhing motion is consistent with the commencement of the impulsive phase of the related flare. The 3D morphology and positions of the associated CME are derived using the graduated cylindrical shell (GCS) modeling. The kinetic evolution of the reconstructed CME is divided into a slow-rise phase ( $\sim 330$  km  $\text{s}^{-1}$ ) and a fast-rise phase ( $\sim 1005$  km  $\text{s}^{-1}$ ) by the writhing motion. The edge-on angular width of the CME is a constant ( $60^\circ$ ), while the face-on angular width increases from  $96^\circ$  to  $114^\circ$ , indicating a lateral expansion. The latitude of the CME source region decreases slightly from  $\sim 18^\circ$  to  $\sim 13^\circ$ , implying an equatorward deflection during propagation.

---

✉ Qingmin Zhang  
zhangqm@pmo.ac.cn

<sup>1</sup> Key Laboratory of Dark Matter and Space Astronomy, Purple Mountain Observatory, CAS, Nanjing 210023, China

<sup>2</sup> School of Astronomy and Space Science, University of Science and Technology of China, Hefei 230026, China

---

**Keywords:** Prominences, Quiescent; Instabilities; Flares; Coronal Mass Ejections

## 1. Introduction

Prominences are cool and dense plasmas suspended in the solar atmosphere (Labrosse et al., 2010; Mackay et al., 2010; Parenti, 2014; Chen, Xu, and Ding, 2020). The materials are formed at magnetic dips due to levitation from below the photosphere (Lites, 2005), direct mass injection (Wang et al., 2019), and catastrophic condensation as a result of thermal instability of evaporated hot plasmas from the chromosphere (Xia et al., 2011; Luna, Karpen, and DeVore, 2012; Zhou et al., 2014; Guo et al., 2021). Two types of magnetic configurations are believed to provide upward tension force to balance the gravity of prominences: sheared arcades (Kippenhahn and Schlüter, 1957; Zhang et al., 2015) and twisted flux ropes (Kuperus and Raadu, 1974; Low and Hundhausen, 1995; Shibata et al., 1995; Rust and Kumar, 1996; Guo et al., 2022). Liu et al. (2012) proposed the scenario of double-decker structures where one flux rope is on top of another flux rope (Hou et al., 2018) or a sheared arcade (Awasthi, Liu, and Wang, 2019). Both of them share a common polarity inversion line (PIL). According to their locations on the solar disk, prominences are divided into quiescent, active region, and intermediate types. Prominences appear not only in  $H\alpha$  (Chae et al., 2008; Zhang et al., 2022a) and  $Ca\ II\ H$  (Berger et al., 2008; Zhang et al., 2012) wavelengths, but also in ultraviolet (UV) and extreme-ultraviolet (EUV) wavelengths (Zou et al., 2019). Prominences are also named filaments consisting of ultrafine dark threads on the disk (Wang et al., 2015, 2018).

Eruptions of small-scale filaments (minifilaments) can lead to blowout coronal jets (Moore et al., 2010; Hong et al., 2013; Li et al., 2015; Sterling et al., 2015; Zhang et al., 2016; Wyper, DeVore, and Antiochos, 2018; Panesar et al., 2022). However, eruptions of large-scale filaments are capable of producing solar flares and coronal mass ejections (CMEs; Chen, 2011; Georgoulis, Nindos, and Zhang, 2019), which are frequently accompanied by EUV waves and coronal dimmings (Thompson et al., 1998; Shen and Liu, 2012; Zhang et al., 2022b). The triggering mechanisms of filament eruptions include magnetic flux emergence (Chen and Shibata, 2000), catastrophic loss of equilibrium of a magnetic flux rope (Lin and Forbes, 2000), tether-cutting of magnetic sheared arcades (Moore et al., 2001; Xue et al., 2017), breakout model (Antiochos, DeVore, and Klimchuk, 1999; Chen et al., 2016), ideal kink instability (Kliem, Titov, and Török, 2004; Török, Kliem, and Titov, 2004; Fan and Gibson, 2003; Fan, 2005; Török and Kliem, 2005), and torus instability (Kliem and Török, 2006). The total twist of a helical flux tube is expressed as (Hood and Priest, 1981; Shen et al., 2011b):

$$\Phi = \frac{LB_\phi(r)}{rB_z(r)}, \quad (1)$$

where  $L$  and  $r$  are the total length and radius of the tube,  $B_\phi(r)$  and  $B_z(r)$  denote the azimuthal and axial components of the magnetic field. The number

of turns over the tube length is (Srivastava et al., 2010; Liu et al., 2016; Jing et al., 2018):

$$\mathcal{T}_w = \frac{1}{4\pi} \int_L \frac{\nabla \times \mathbf{B} \cdot \mathbf{B}}{B^2} dl = \frac{\Phi}{2\pi}. \quad (2)$$

The critical values of  $\Phi_c$  for kink instability ranges from  $2.5\pi$  to  $3.5\pi$  under different circumstances (Hood and Priest, 1981; Török and Kliem, 2003; Török, Kliem, and Titov, 2004; Kliem, Török, and Thompson, 2012). Observational evidences of helical kink instability are substantial in failed eruptions (e.g., Ji et al., 2003; Alexander, Liu, and Gilbert, 2006; Liu, Alexander, and Gilbert, 2007; Liu and Alexander, 2009; Guo et al., 2010; Amari et al., 2018), partial eruptions (Tripathi et al., 2013), and successful eruptions (e.g., Williams et al., 2005; Cho et al., 2009; Kumar et al., 2012; Cheng et al., 2014a; Vemareddy, Gopalswamy, and Ravindra, 2017). The total twist is reported to be between  $3.6\pi$  and  $12\pi$ , part of which is converted into writhe during eruption (Gilbert, Alexander, and Liu, 2007; Török, Berger, and Kliem, 2010). The sense of twist should be the same as the writhe (Rust and LaBonte, 2005). Therefore, rapid rotation of filament legs or spines is frequently observed (Green et al., 2007; Liu, Alexander, and Gilbert, 2007; Bemporad, Mierla, and Tripathi, 2011; Kliem, Török, and Thompson, 2012; Su and van Ballegooijen, 2013; Yan et al., 2014a).

As mentioned above, filament eruptions could drive CMEs. The kinematic and morphological evolutions of CMEs in the three-dimensional (3D) space is essential for a precise determination of the arrival times of halo CMEs (Liu et al., 2010). To this end, various kinds of cone models were proposed assuming an ice-cream shape and a constant speed of a CME (e.g., Howard et al., 1982; Zhao, Plunkett, and Liu, 2002; Michałek, Gopalswamy, and Yashiro, 2003; Xie, Ofman, and Lawrence, 2004; Xue, Wang, and Dou, 2005). These models have achieved great success in reconstructing the 3D morphology and tracking the propagation of earthward CMEs in the corona and interplanetary space. Recently, Zhang (2021) put forward a revised cone model to explain non-radial prominence eruptions. The model is gratifyingly applied to tracking the 3D evolution of a halo CME due to the non-radial eruption of a flux rope on 21 June 2011 (Zhang, 2022). Considering the flux-rope nature of CMEs (Cremades and Bothmer, 2004; Krall and St. Cyr, 2006), a new technique was developed to model the flux-rope like CMEs by using the graduated cylindrical shell (GCS) model (Thernisien, Howard, and Vourlidas, 2006; Thernisien, Vourlidas, and Howard, 2009; Thernisien, 2011). This model is mainly characterized by three geometric parameters ( $\alpha$ ,  $h$ , and  $\kappa$ ) and three positioning parameters ( $\phi$ ,  $\theta$ , and  $\gamma$ ), which will be described in detail in Sect. 3.2. This technique has widely been used to investigate the geometrical and kinematic evolutions of CMEs viewed from two or three perspectives (Mierla et al., 2009; Liu et al., 2018; Cremades, Iglesias, and Merenda, 2020; Gou et al., 2020; Majumdar et al., 2020; Majumdar, Patel, and Pant, 2022).

Cheng et al. (2013) studied the eruptions of two successive magnetic flux ropes as a result of ideal torus instability and performed 3D reconstructions of the associated CMEs using GCS modeling. Furthermore, Cheng et al. (2014b) tracked the evolution of a magnetic flux rope from the inner to the outer corona

and found that the impulsive acceleration phase of the flux rope is caused by the torus instability. The 3D morphology of the associated CME was also obtained using GCS modeling. So far, 3D reconstructions of CMEs caused by the eruption of flux ropes due to kink instability have rarely been reported. In this paper, we carry out a detailed investigation of the rapid rotation of an erupting quiescent prominence and the associated CME occurring in the northern hemisphere on 13 May 2013. The prominence originates from the farside near the western limb, and the rotation is found to result from kink instability. Meanwhile, we carry out a 3D reconstruction of the associated CME using the GCS modeling. The paper is organized as follows. We describe the data analysis in Section 2. The results are presented in Section 3 and compared with previous findings in Section 4. Finally, a brief summary is given in Section 5.

## 2. Data Analysis

The prominence eruption was observed by the Atmospheric Imaging Assembly (AIA; Lemen et al., 2012) on board the Solar Dynamics Observatory (SDO; Pesnell, Thompson, and Chamberlin, 2012) spacecraft. SDO/AIA takes full-disk images in seven EUV wavelengths (94, 131, 171, 193, 211, 304, 335 Å) and two UV wavelengths (1600 and 1700 Å). The AIA level.1 data were calibrated using the standard Solar Software (SSW) program `aia_prep.pro`. The prominence was also observed in 174 Å ( $\log T \approx 5.8$ ) by the Sun Watcher using Active Pixel System detector and image processing (SWAP; Berghmans et al., 2006; Seaton et al., 2013) on board the PROBA 2 spacecraft with a larger field of view (FOV) than AIA.

The event was simultaneously captured by the ahead and behind Solar Terrestrial Relations Observatory (STEREO; Kaiser et al., 2008) spacecraft from two perspectives. Figure 1 shows the positions of the Earth, Ahead (A), and Behind (B) STEREO spacecraft on 13 May 2013. The separation angles of STEREO-A and STEREO-B with the Earth were  $\sim 136^\circ$  and  $\sim 142^\circ$  (Gou et al., 2020). Consequently, the large prominence close to the western limb in the FOV of AIA appeared as a prominence close to the eastern limb in the FOV of behind Extreme-UltraViolet Imager (EUVI; Wuelser et al., 2004) of the Sun Earth Connection Coronal and Heliospheric Investigation (SECCHI; Howard et al., 2008) and appeared as a long filament in the FOV of ahead EUVI. This provides a unique opportunity to study the prominence eruption from three perspectives simultaneously (Cheng et al., 2014b). EUVI takes full-disk images out to  $1.7 R_\odot$  in 171, 195, 284, and 304 Å. The images were calibrated using the SSW program `secchi_prep.pro`.

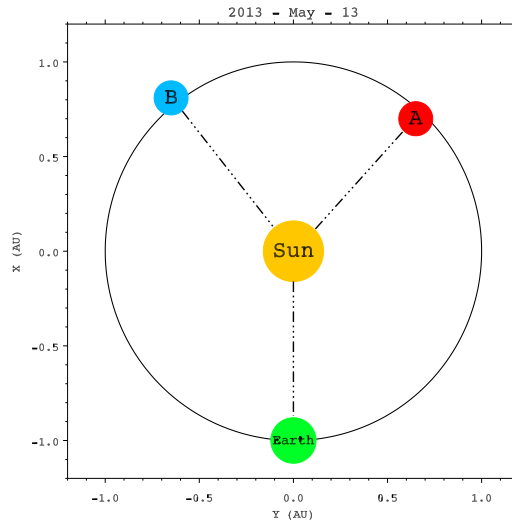
The associated CME was observed by the Large Angle Spectroscopic Coronagraph (LASCO; Brueckner et al., 1995) on board SOHO spacecraft and recorded by the CDAW CME catalogue<sup>1</sup>. The LASCO-C2 and LASCO-C3 white light (WL) coronagraphs have FOVs of  $2-6 R_\odot$  and  $4-30 R_\odot$ , respectively. The CME

---

<sup>1</sup><http://cdaw.gsfc.nasa.gov/CME.list>

**Table 1.** Description of the observational parameters.

Instrument	$\lambda$ [Å]	Time [UT]	Cadence [s]	Pixel Size ['']
AIA	171, 304	13:30–18:30	12	0.6
SWAP	174	17:09–17:51	130	3.2
STA/EUVI	195	13:30–20:30	300	1.6
STA/EUVI	304	13:30–20:30	600	1.6
STA/EUVI	284	13:30–20:30	7200	1.6
STB/EUVI	304	13:30–20:30	600	1.6
COR1	WL	17:15–18:20	900	14.7
COR2	WL	17:30–20:00	900	14.7
LASCO/C2	WL	17:24–19:36	720	11.4
LASCO/C3	WL	18:18–19:54	720	56.0
GOES	0.5–4	15:00–18:00	2.05	...
GOES	1–8	15:00–18:00	2.05	...


**Figure 1.** Positions of the Earth, Ahead (A), and Behind (B) STEREO spacecrafts at 00:55 UT on 13 May 2013.

was also detected by the COR1 and COR2 coronagraphs on board STEREO-A and STEREO-B, which enables 3D reconstruction using the GCS modeling. Soft X-ray (SXR) light curves of the Sun in 1–8 Å and 0.5–4 Å were recorded by the Geostationary Operational Environmental Satellite (GOES) spacecraft. The observational parameters are listed in Table 1.

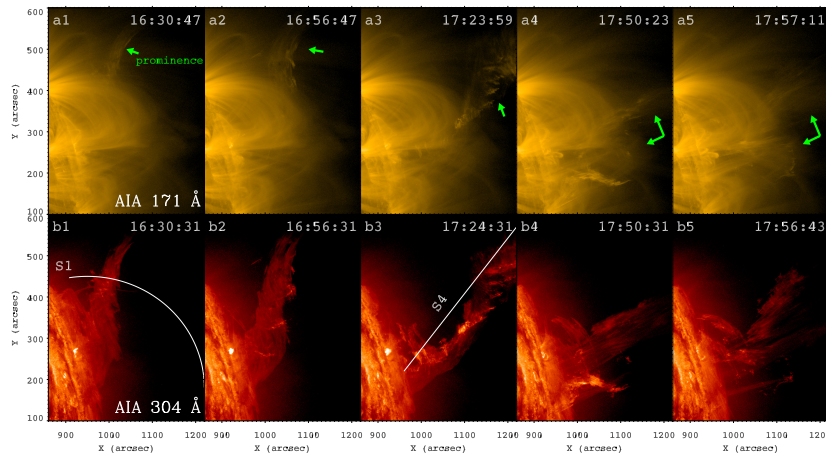


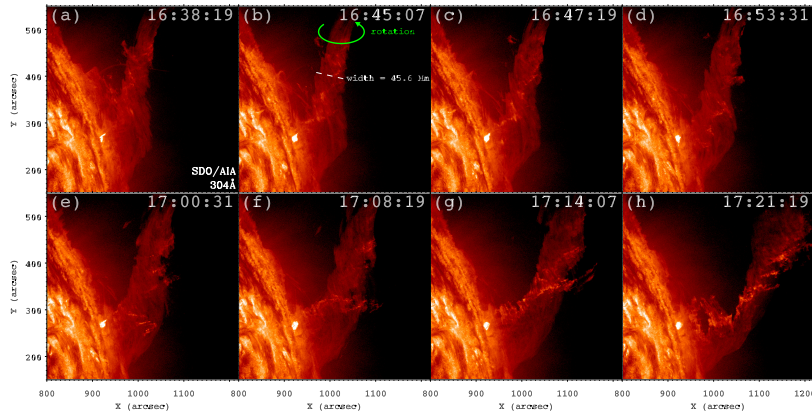
**Figure 2.** Selected 171 Å (top panels) and 304 Å (bottom panels) images observed by SDO/AIA during the prominence eruption, respectively. In panel (b1), the curved slice S1 is used to investigate the rapid rotation and drift motion. In panel (b3), the straight slice S4 is used to investigate the rising motion. An animation of this figure is available in the Electronic Supplementary Material ([anim1.mp4](#)).

### 3. Results

#### 3.1. Prominence Eruption and the associated CME

In Figure 2, the top and bottom panels show 171 Å and 304 Å images observed by SDO/AIA (see also online animation [anim1.mp4](#)). The prominence rises from the farside and appears above the western limb. Rapid rotation of the prominence body is obvious during prominence eruption (16:34–17:21 UT). Figure 3 shows eight snapshots of the prominence during 16:38–17:21 UT. In panel (b), the white dashed line across the prominence is used to measure the width ( $D$ ) of prominence, being  $\sim 45.6$  Mm. Assuming a cylindrical shape of the prominence, the radius is  $\sim 22.8$  Mm.

The online movie ([anim1.mp4](#)) indicates that the direction of rotation is counterclockwise viewed from above. Figure 4 shows snapshots of the prominence observed by AIA in 304 Å. We tracked some of the bright features in the foreground during rotation, which are marked with blue and white circles. It is clear that the prominence is rotating counterclockwise. Contrary to the rotating jets whose axes are almost static (e.g., Curdt and Tian, 2011; Shen et al., 2011b; Chen, Zhang, and Ma, 2012; Hong et al., 2013; Schmieder et al., 2013; Zhang and Ji, 2014), the prominence rises and drifts southwestward during rotation. To investigate the rotation in detail, we choose a curved slice (S1) across the leg in Figure 2(b1). The time-slice diagram of S1 in 304 Å is displayed in Figure 5(a). The sinusoidal patterns (light blue dots) in the inset indicate rapid rotation during 16:34–17:21 UT (Okamoto, Liu, and Tsuneta, 2016). Therefore, the rotation lasts for  $\sim 47$  minutes. The seven green arrows point to the bright features that appear periodically. The corresponding 304 Å images at these moments are displayed in Figure 3. The average period ( $P$ )



the green arrow indicates the counterclockwise direction of rotation viewed from above. The white dashed line is used to measure the width (45.6 Mm) of prominence.

**Figure 3.** Snapshots of the rotating prominence observed by AIA in 304 Å during 16:38–17:21 UT. In panel (b),

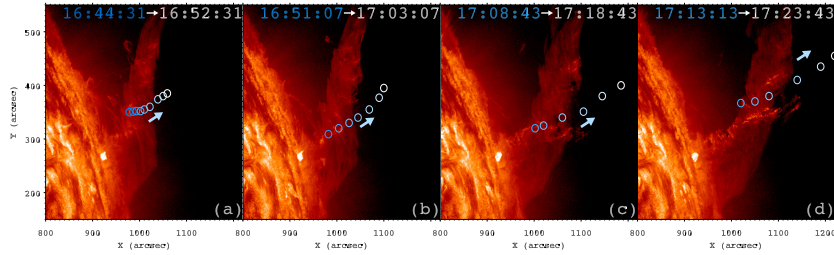
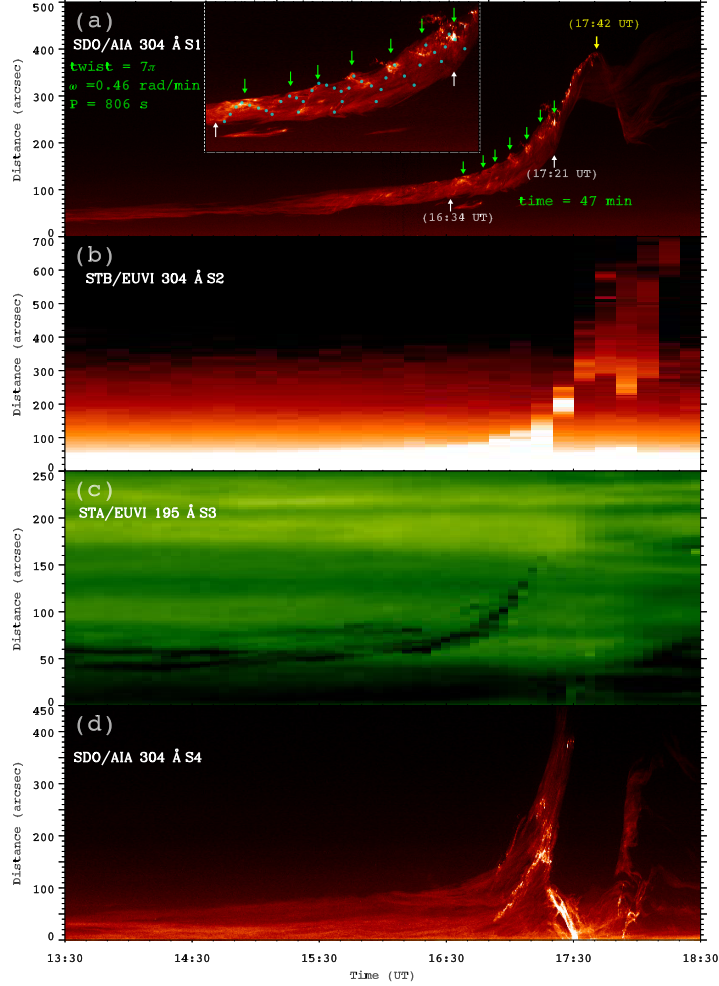


**Figure 4.** Snapshots of the prominence observed by AIA in 304 Å. The circles denote the trajectories of bright features in the foreground during the rotation. On top of each panel, the time in blue corresponds to the observing time of the EUV image.

is calculated to be  $\sim 806$  s, and the corresponding angular speed ( $\omega$ ) is  $\sim 0.46$  rad  $\text{min}^{-1}$ . Considering the width of the prominence in Figure 3(b), the linear speed is  $v = \omega D/2 \approx 355$  km  $\text{s}^{-1}$ . The total angle of rotation reaches  $\sim 7\pi$ , which significantly exceeds the critical twist for kink instability (Hood and Priest, 1981; Török and Kliem, 2003; Török, Kliem, and Titov, 2004). Accordingly, the rapid rotation is indicative of untwisting motion of a highly twisted prominence. In Figure 5(a), the yellow arrow denotes the turning point ( $\sim 17:42$  UT) when the direction of drift reverses, which implies the writhing motion (Fan and Gibson, 2003; Török and Kliem, 2005; Liu, Alexander, and Gilbert, 2007). It should be noted that rotation in the clockwise direction near the footpoint of prominence is observed during 17:40–18:05 UT. Such reversal of direction of prominence rotation has been reported by Thompson, Kliem, and Török (2012) and Song et al. (2018). This short period of rotation is not considered when calculating the total twist of the prominence.



The values of total twist ( $\Phi = 7\pi$ ), average angular speed ( $\omega = 0.46 \text{ rad min}^{-1}$ ) and period ( $P = 806 \text{ s}$ ) are labeled. (b) Time-slice diagram of S2 in STB/EUVI 304 Å. (c) Time-slice diagram of S3 in STA/EUVI 195 Å. (d) Time-slice diagram of S4 in AIA 304 Å.

**Figure 5.** (a) Time-slice diagram of S1 in AIA 304 Å.  $s = 0$  and  $s = 500''$  represent the northeast and southwest endpoints of S1, respectively. The white arrows indicate the start and end times of prominence rotation, which lasts for  $\sim 47$  minutes. The green arrows point to the bright features. The yellow arrow denotes the turning point when the direction of drift reverses. The inset shows an enlarged view of the time-slice diagram during rotation. The light blue dots outline the sinusoidal patterns.



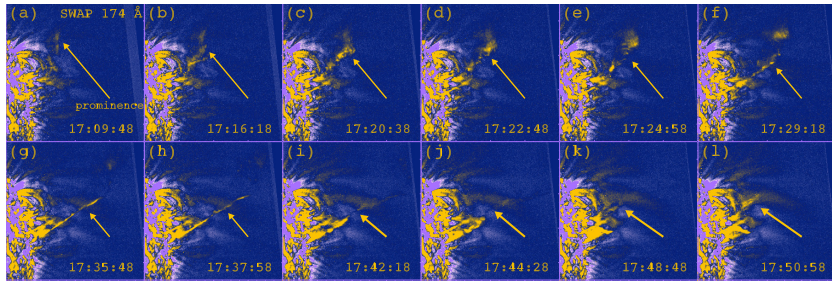


**Figure 6.** Base-difference images of the erupting prominence observed by SWAP in 174 Å. The FOV is  $800'' \times 800''$ . The yellow arrows point to the prominence. An animation of this figure is available in the Electronic Supplementary Material ([anim2.mp4](#)).

To investigate the rising motion of the prominence, we choose a straight slice (S4) in Figure 2(b3). The time-slice diagram of S4 in 304 Å is displayed in Figure 5(d). The prominence undergoes a prolonged slow rise phase and a fast rise phase. The fast rise starts from  $\sim 16:50$  UT until 17:30 UT when the upper part escapes the FOV of AIA to drive a CME.

The eruption was captured by SWAP in 174 Å with a larger FOV. Figure 6 shows a series of base-difference images (see also the online animation [anim2.mp4](#)). The prominence, which is indicated by the arrows, starts to rise at  $\sim 17:09$  UT, accompanied by southwestward drift until  $\sim 17:42$  UT (panels (a-i)). Afterward, the direction of drift reverses, suggesting the writhing motion (panels (j-l)).

As mentioned in Sect. 1, the twin STEREO spacecraft observed the event from two perspectives. Figure 7 shows a series of 304 Å images observed by STB/EUVI (see also the online animation [anim3.mp4](#)). The prominence, which is indicated by the white arrow, elevates slowly from  $\sim 17:00$  UT and experiences a clear writhing motion around 17:46 UT with an “inverted  $\gamma$ ” shape, which is indicated by the green arrow in panel (f). The top of the prominence when kink instability takes place at 17:46:42 UT is  $\sim 405$  Mm ( $0.58 R_{\odot}$ ) above the solar limb. Using triangulation method, the true height is estimated to be  $\sim 488$  Mm ( $0.70 R_{\odot}$ ). Afterward, the prominence continues to rise and escapes the FOV of STB/EUVI (panels (g-h)). To investigate the height evolution, a straight slice (S2) is selected in panel (e). The time-slice diagram of S2 is plotted in Figure 5(b). The height evolution is also characterized by a slow rise phase and a fast rise phase, which are in agreement with the trend in AIA 304 Å (Figure 5(d)).

The bright prominence manifests itself as a dark filament in the FOV of STA/EUVI. Figure 8 shows 195 Å images observed by STA/EUVI. The filament starts to rise at  $\sim 17:00$  UT until  $\sim 17:35$  UT when the spine of filament becomes undistinguishable (panel (e)). The southwest footpoint of the filament drifts and generates a hooklike dimming region close to an equatorial coronal hole (Wang et al., 2017; Aulanier and Dudík, 2019; Lörinčík et al., 2021). The eruption generates a pair of bright flare ribbons (R1 and R2), which undergo separation.

Figure 9 shows 304 and 284 Å images observed by STA/EUVI. The evolution of filament and flare ribbons in 304 Å is analogous to that in 195 Å. The bright

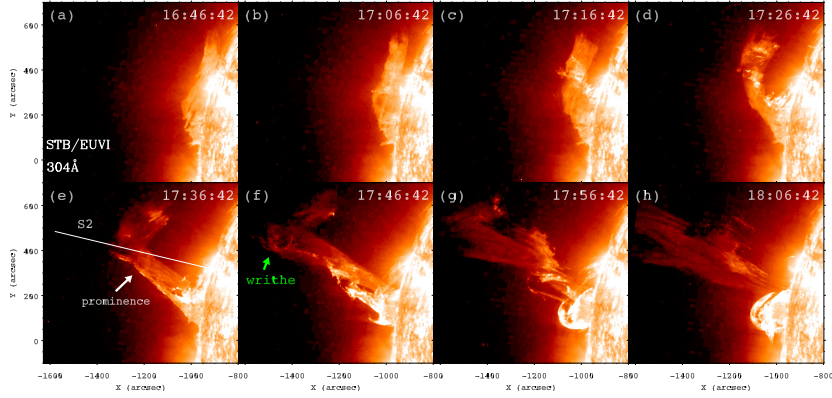


**Figure 7.** EUV 304 Å images of the erupting prominence observed by STB/EUVI. In panel (e), a straight slice (S2) is used to investigate the height evolution of prominence. In panel (f), the green arrow indicates the writhe of prominence. An animation of this figure is available in the Electronic Supplementary Material (anim3.mp4).

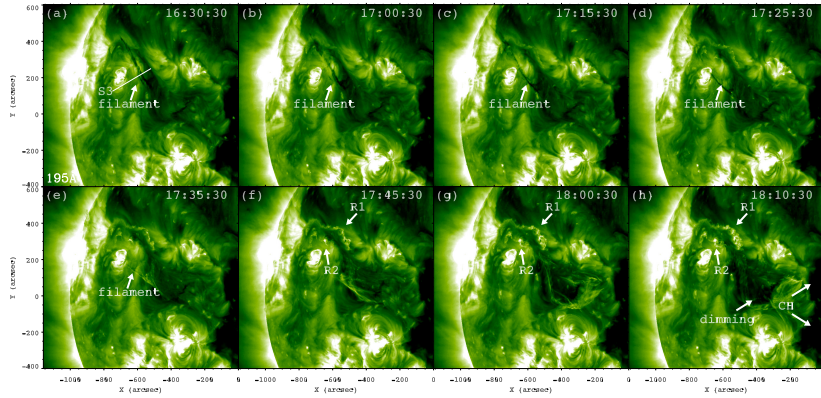


**Figure 8.** EUV 195 Å images of the rising filament observed by STA/EUVI. The arrows point to the dark filament, bright flare ribbons (R1 and R2), hooklike dimming, and an equatorial coronal hole (CH).

post flare loops connecting the ribbons are captured in 284 Å ( $\log T \approx 6.3$ ) in panel (h). In panel (g), two representative boxes ( $3'' \times 3''$ ) at the conjugate flare ribbons are selected. The normalized total intensities of the boxes are plotted in Figure 10(a-b). The EUV intensities increase from  $\sim 17:30$  UT and peak at 18:00–18:20 UT followed by a gradual decay. The blue dashed line denotes the onset time ( $\sim 17:42$  UT) of kink instability, which is consistent with the beginning of the flare impulsive phase. For comparison, the SXR light curves in 1–8 Å and 0.5–4 Å during 15:00–18:00 UT are plotted with red and cyan lines in Figure 10(c). The huge enhancements of SXR emission starting at 15:48 UT and peaking at 16:05 UT originate from the X2.8 class flare in NOAA active region 11748 close to the eastern limb (Gou et al., 2020). There is no SXR response of the flare ribbons observed in 304 Å by STA/EUVI, meaning that the flare completely occurred at the farside.

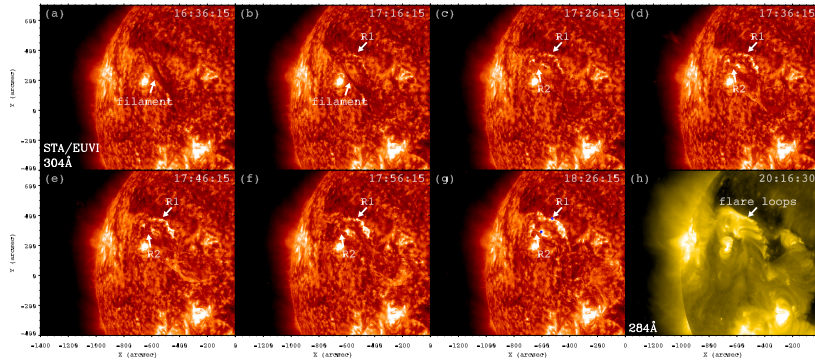


**Figure 9.** EUV 304 and 284 Å images of the rising filament observed by STA/EUVI. The arrows point to the dark filament, bright flare ribbons (R1 and R2), and post flare loops. In panel (g), two blue boxes are used to calculate the total intensities of R1 and R2.

**Table 2.** Parameters of the CME observed by the WL coronagraphs on board LASC0, STB, and STA. For comparison, the values of AW and  $V$  from the GCS modeling are listed in the last column.

Spacecraft	LASC0	STB	STA	GCS
Instrument	C2, C3	COR1, COR2	COR1, COR2	—
$t_0$ (UT)	17:24	17:10	17:25	—
PA ( $^\circ$ )	$\sim 288$	$\sim 72$	$\sim 74$	—
AW ( $^\circ$ )	$\sim 82$	$\sim 77$	$\sim 82$	$\sim 114$
$V$ ( $\text{km s}^{-1}$ )	$\sim 844$	$\sim 762$	$\sim 837$	$\sim 1005$

As mentioned in Sect. 1, the eruption drives a fast CME. The running-difference images of the CME observed by LASC0-C2 are displayed in Figure 11. The CME first appears at  $t_0 = 17:24$  UT and rises up in the northwest direction, showing a typical three-part structure: a bright leading edge, a dark cavity, and a bright core (panels (c-d)). The core is widely believed to consist of an erupting prominence, which is presented in Figure 2 (Liu, Alexander, and Gilbert, 2007; Song, Li, and Chen, 2022). The CME propagates further until 20:06 UT in the FOV of LASC0-C3 (Figure 12), and the height evolution is drawn with blue diamonds in Figure 10(d). The fitted linear speed ( $V$ ) is  $\sim 844 \text{ km s}^{-1}$ . The parameters, including  $t_0$ , position angle (PA), final angular width (AW), and  $V$  of the CME observed by LASC0, are listed in the second column of Table 2.

Likewise, the running-difference images of the CME in the FOV of COR1 and COR2 on board STB are displayed in Figure 13 and Figure 14, respectively. The CME first appears at 17:10 UT with the same three-part morphology and propagates in the northeast direction until 20:09 UT at a speed of  $\sim 762 \text{ km s}^{-1}$  (see the third column of Table 2). The running-difference images of the CME in the FOV of COR1 and COR2 on board STA are displayed in Figure 15 and Figure 16, respectively. The CME first appears at 17:25 UT and propagates in the northeast direction until 20:24 UT at a speed of  $\sim 837 \text{ km s}^{-1}$  (see the fourth

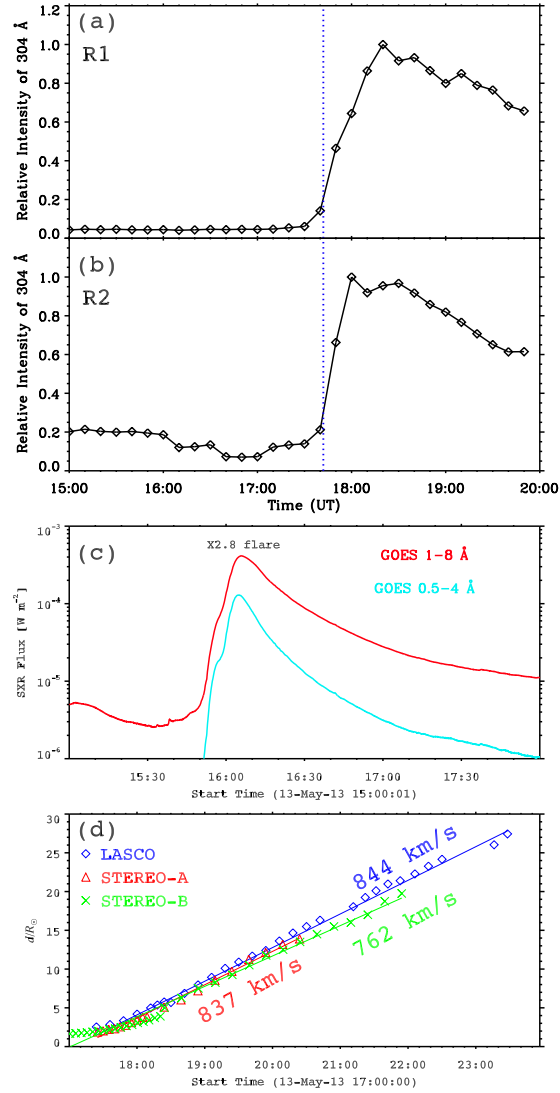


**Figure 10.** (a-b) Normalized total intensities of the flare ribbons (R1 and R2). The blue dashed line denotes the onset time ( $\sim 17:42$  UT) of kink instability. (c) SXR light curves during 15:00–18:00 UT. (d) Height evolutions of the CME LE observed by LASCO (blue diamonds), STA (red triangles), and STB (green crosses), respectively. The corresponding linear speeds are labeled.

column of Table 2). The WL intensities of CME get too weak to be identified after 20:30 UT. After checking the WL images of the CME carefully, we conclude that the CME is not a Cartwheel CME, which carries away a part of the twist and consequently shows highly visible rotation around the line of sight (Thompson, Kliem, and Török, 2012; Pant et al., 2018).

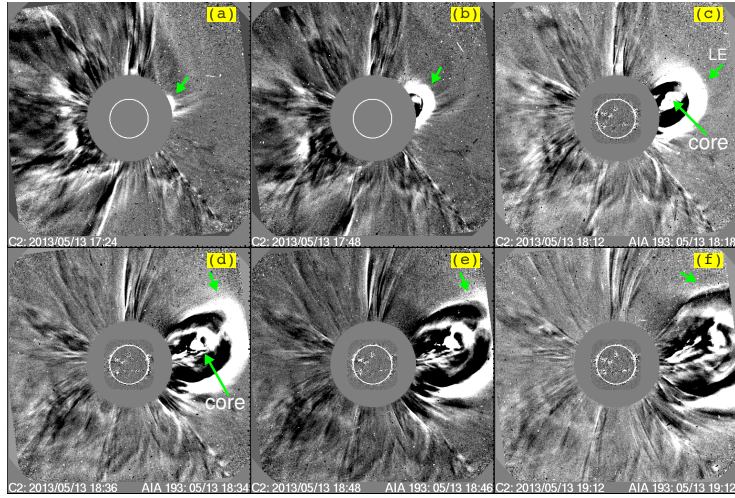


**Figure 11.** Running-difference images of the CME observed by LASCO-C2. The green arrows indicate the CME leading edge (LE) and core.

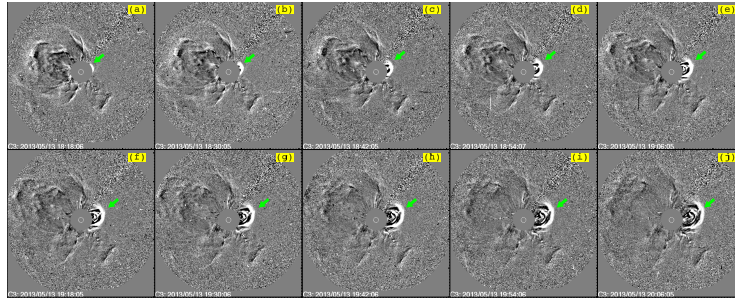


**Figure 12.** Running-difference images of the CME observed by LASCO-C3. The green arrows indicate the CME leading edge (LE).

### 3.2. 3D Reconstruction of the CME using GCS modeling

Simultaneous observations of the CME enable us to perform a 3D reconstruction of the CME. Although the CME LE shows a nearly symmetric bubble in the FOVs of LASCO and STB, it looks raised and irregular in the FOV of STA/COR2, which is unsuitable for cone models (Michalek, Gopalswamy, and Yashiro, 2003; Zhang, 2021). Considering the helical structure and rapid rotation of the prominence (Figures 2 and 3), it is concluded that the CME is driven by a highly twisted magnetic flux rope. Naturally, we turn to the GCS modeling (Thernisien, Howard, and Vourlidas, 2006). The GCS, resembling a croissant, is composed of two conical “legs” with angular separation of  $2\alpha$  and a circular annulus of varying radius:

$$a(r) = \kappa r, \quad (3)$$

where  $r$  is the distance from the Sun center to a point at the outer edge of the shell, and  $\kappa$  is the CME aspect ratio. Each leg has a height of  $h$  and half angle

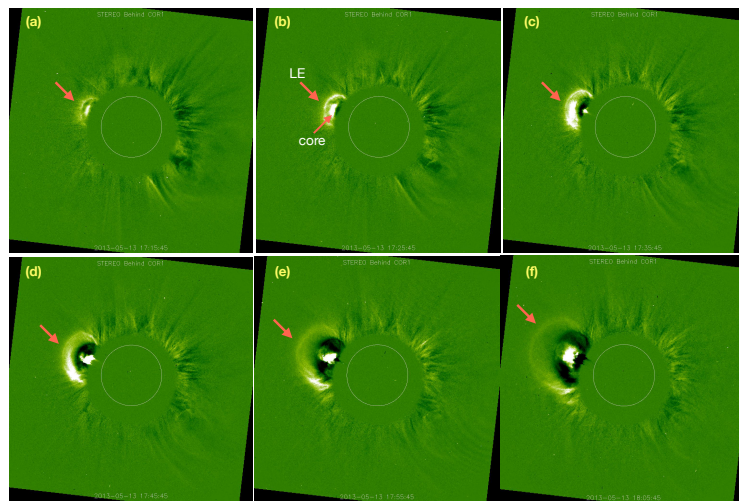


**Figure 13.** Running-difference images of the CME observed by STB/COR1. The orange arrows indicate the CME leading edge (LE) and core.

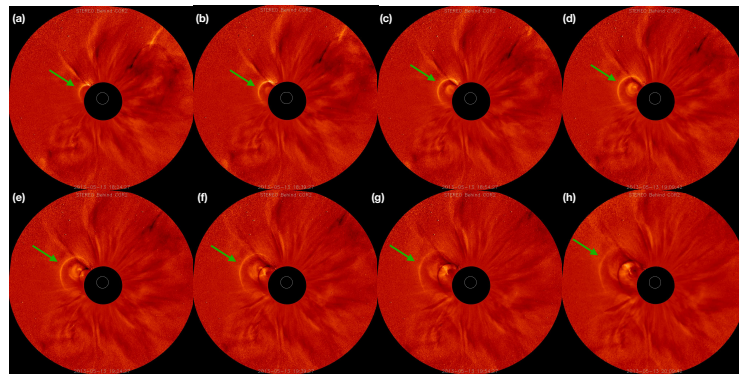


**Figure 14.** Running-difference images of the CME observed by STB/COR2. The green arrows indicate the CME leading edge (LE).

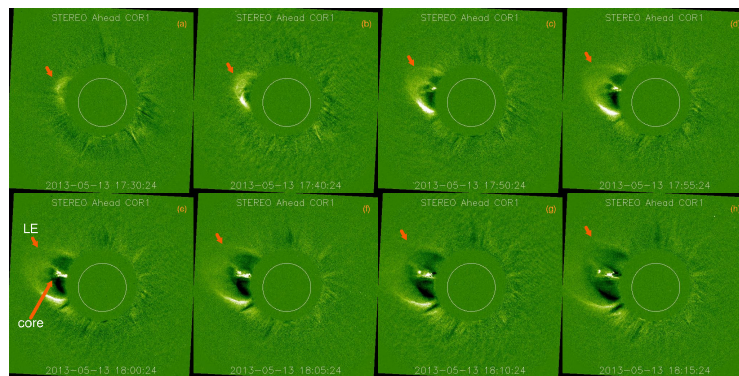


**Figure 15.** Running-difference images of the CME observed by STA/COR1. The orange arrows indicate the CME leading edge (LE) and core.

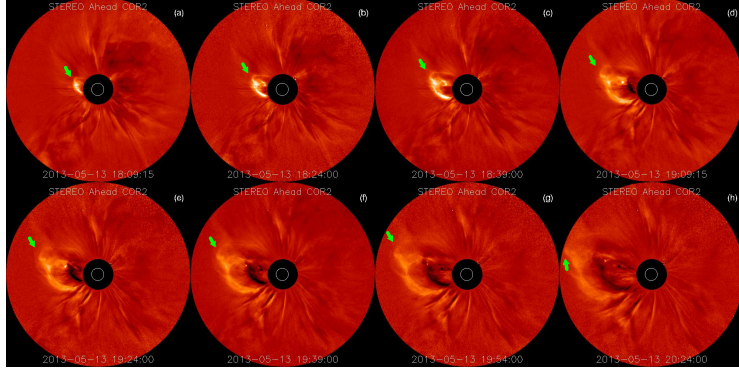


**Figure 16.** Running-difference images of the CME observed by STA/COR2. The green arrows indicate the CME leading edge (LE).

of  $\delta$  (Thernisien, 2011):

$$\kappa = \sin \delta. \quad (4)$$

Two auxiliary parameters are:

$$b = h / \cos \alpha, \quad (5)$$

$$\rho = h \tan \alpha. \quad (6)$$

Accordingly, the heliocentric height of the LE is:

$$h_{\text{LE}} = \frac{b + \rho}{1 - \kappa} = \frac{h}{1 - \kappa} \left( \frac{1}{\cos \alpha} + \tan \alpha \right). \quad (7)$$

The edge-on and face-on angular widths are:

$$\omega_{\text{EO}} = 2\delta, \quad (8)$$

$$\omega_{\text{FO}} = 2(\alpha + \delta) = 2\alpha + \omega_{\text{EO}}. \quad (9)$$

The source region of the CME has a Carrington longitude  $\phi$  and a latitude  $\theta$ . The tilt angle of the PIL is denoted by  $\gamma$ . Since the eruption of large-scale prominence occurs at the farside, the value of  $\phi$  is changed repeatedly and eventually set to be  $91^\circ$ . The value of  $\theta$  changes slightly to derive a better fitting, although it should be fixed if the CME does not experience a deflection (see Figure 19(c)). The value of  $\gamma = 45^\circ$  is roughly determined from the STA/EUVI images in Figure 9. The value of  $\kappa$  is set to be 0.5 ( $\delta = 30^\circ$ ) after many trials. As the CME expands laterally, the value of  $\alpha$  increases.

To perform GCS modeling, we use WL images of the CME observed by LASCO and STA. Considering the inconsistency in time cadence between the two spacecrafts, we first use images, preferably at the same time. Figure 17 shows a series of images of the CME observed by LASCO and STA during 17:24–19:54 UT. The reconstructed GCS models are projected with red-violet

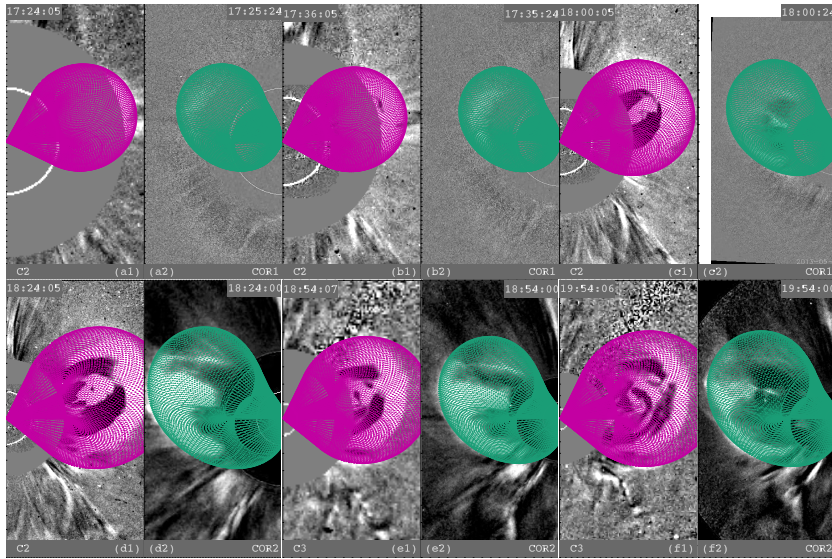


**Figure 17.** Selected WL images of the CME observed by LASCO and STA almost simultaneously, which are overlaid with reconstructed GCS models (red-violet and blue-green dots).

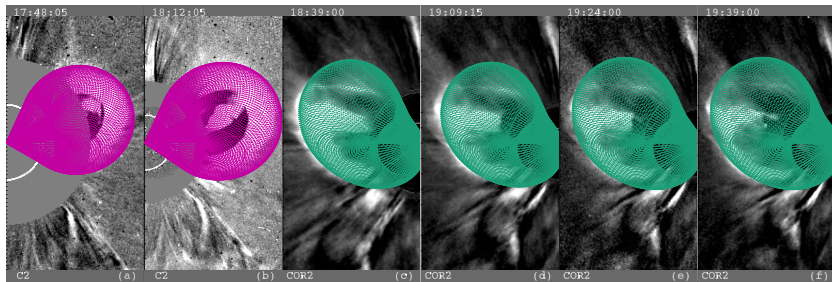


**Figure 18.** Selected WL images of the CME observed by LASCO (a-b) and STA (c-f), which are overlaid with reconstructed GCS models (red-violet and blue-green dots).

and blue-green dots, respectively. It is clear that the GCS models fit well with the observations. The leading edges of the CME are perfectly consistent with those of GCS models. Time evolutions of the height ( $h$ ), face-on angular width ( $\omega_{FO}$ ), edge-on angular width ( $\omega_{EO}$ ),  $2\alpha$ , and  $\theta$  are plotted in Figure 19. For those not simultaneously observed by LASCO and STA, we use WL images from one perspective for reconstruction. Figure 18 shows a series of images of the CME observed by LASCO (a-b) and STA (c-f), which are overlaid with the GCS models (red-violet and blue-green dots), indicating that the fittings are still satisfactory.

The results of fittings are plotted in Figure 19. The separation angle of the legs (red triangles in panel (c)) and the face-on angular width (cyan squares in panel (b)) increase sharply from  $\sim 17:24$  UT to  $\sim 17:36$  UT, implying a quick lateral expansion (Patsourakos, Vourlidas, and Stenborg, 2010; Cremades, Iglesias,



and Merenda, 2020; Majumdar et al., 2020; Majumdar, Patel, and Pant, 2022). Afterwards, the two parameters increase gradually until  $\sim 18:24$  UT and nearly keep constant ( $54^\circ$  and  $114^\circ$ ). The maximum of  $\omega_{\text{FO}}$  is larger than the apparent widths of CME in each coronagraph (see Table 2). The final ratio  $\frac{\omega_{\text{FO}}}{\omega_{\text{EO}}}$  is equal to 1.9, which is consistent with the value reported by Krall and St. Cyr (2006) and the average value ( $1.84 \pm 0.37$ ) of the 12 events reported by Cremades, Iglesias, and Merenda (2020). Recently, Majumdar, Patel, and Pant (2022) investigated the rapid initial acceleration and width expansion of five CMEs at lower heights using the GCS modeling. It is found that the face-on widths expand faster than the edge-on widths (see their Fig. 3), which is in agreement with our finding. The latitude  $\theta$  decreases slightly from  $18^\circ$  at 18:00 UT to  $13^\circ$  at 18:24 UT, suggesting an equatorward deflection during propagation (Byrne et al., 2010; Gui et al., 2011; Shen et al., 2011a; Liu et al., 2018; Majumdar et al., 2020).

The leg height  $h$  increases from  $\sim 638$  Mm at 17:24 UT to  $\sim 3081$  Mm at 19:54 UT, and the leading edge height  $h_{\text{LE}}$  increases from  $\sim 2.5R_\odot$  to  $\sim 14.5R_\odot$ . The final speed ( $\sim 1005 \text{ km s}^{-1}$ ) in 3D is greater than the apparent speeds of CME in each coronagraph (see Figure 19(a) and Table 2). Although the CME is fast and wide enough, which is capable of driving an interplanetary shock (Morosan et al., 2019; Zhang et al., 2022b), no type II radio burst was detected by the ground-based radio stations<sup>2</sup>. This is probably due to that the CME originates from the farside and propagates away from the Earth.

In Figure 20, the 3D view of the Sun (colored dots) and reconstructed GCS (blue dots) at 19:54 UT from perspectives of SOHO/LASCO (a), STA/COR1 (b), and solar north (c) are presented (see also the online animation [anim4.mp4](#)).

#### 4. Discussion

Prominences are rich in dynamics, such as large-amplitude oscillations (Zhang et al., 2012; Kucera et al., 2022), upflows and downflows (Berger et al., 2008). Rotations are also ubiquitous, not only in magnetized tornados (Pettit, 1943; Su et al., 2012, 2014; Wedemeyer-Böhm et al., 2012; Luna, Moreno-Insertis, and Priest, 2015; Yang et al., 2018) but also in erupting prominences (Thompson, 2011; Thompson, Kliem, and Török, 2012; Liu et al., 2015; Song et al., 2018). Interestingly, the direction of prominence rotation may reverse during the ascending phase (Thompson, Kliem, and Török, 2012; Song et al., 2018). There are at least three reasons for rotation in erupting prominences. The first is ideal kink instability when the magnetic twist exceeds the threshold (Yan et al., 2014a,b). The second is twist transfer during magnetic reconnection between a highly twisted prominence and less twisted coronal loops (Shibata and Uchida, 1986; Kurokawa et al., 1987; Li et al., 2016; Okamoto, Liu, and Tsuneta, 2016; Xue et al., 2016; Yan et al., 2020). The third is the roll effect if a filament erupts non-radially (Martin, 2003; Panasenco and Martin, 2008; Panasenco et al., 2013). The top of the filament ribbon bends toward or away from the observer. As

---

<sup>2</sup><https://www.e-callisto.org>

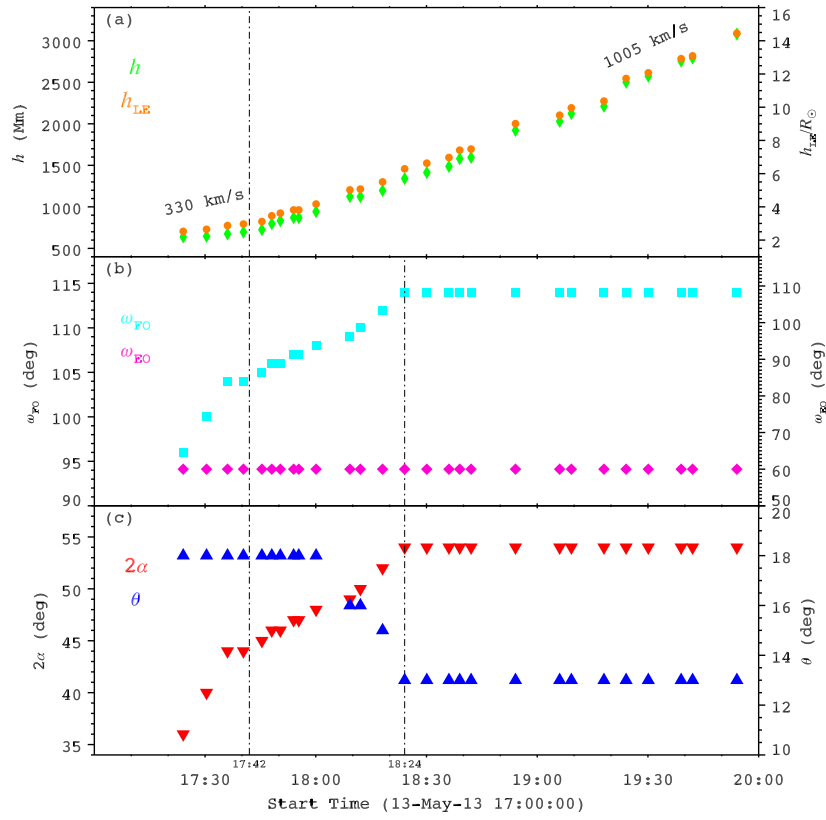


**Figure 19.** Time evolutions of the leg height ( $h$ ), leading ledge height ( $h_{LE}$ ), face-on angular width ( $\omega_{FO}$ ), edge-on angular width ( $\omega_{EO}$ ), angular separation ( $2\alpha$ ) of the legs, and latitude ( $\theta$ ). The left dot-dashed line denotes the onset time (17:42 UT) of the writhing motion. The right dot-dashed line denotes the time (18:24 UT) when  $2\alpha$  and  $\omega_{FO}$  reach the maxima. In panel (a), the linear speeds before and after 17:42 UT are labeled.

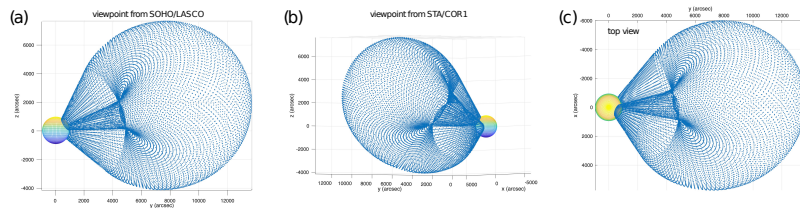


**Figure 20.** Viewpoints of the Sun (colored dots) and reconstructed GCS (blue dots) from SOHO/LASCO (a), STA/COR1 (b), and solar north at 19:54 UT, respectively. An animation of this figure is available in the Electronic Supplementary Material (anim4.mp4).

**Table 3.** Comparison between the ideal kink instability and roll effect.

	kink instability	roll effect
shape of filament	twisted flux rope	ribbon-like
initiation	pre-stored twist	bending at the top
chirality of two legs	same	opposite
rotation directions of two legs	same	opposite
writhing motion	yes	no

a consequence, the rolling motion propagates down the two legs of filaments simultaneously, generating significant twists in the legs with opposite chirality. That is to say, the two legs rotate in opposite directions (see Fig. 2 in Panasenco et al. (2013)). Specifically, dextral filaments have a rolling motion toward the observer, which is accompanied by counterclockwise (clockwise) rotation at the left (right) leg, respectively. Sinistral filaments have a rolling motion away from the observer, which is accompanied by counterclockwise (clockwise) rotation at the right (left) leg (see Fig. 4 in Panasenco and Martin (2008)). In Table 3, we compare the ideal kink instability with roll effect in detail, which are different at least in five aspects, including the shape of filament, initiation, chirality and rotation directions of two legs, and writhing motion.

In our study, the rising prominence keeps rotating in the counterclockwise direction for  $\sim 47$  minutes with an average period of  $\sim 806$  s (Figure 5). The total angle of rotation reaches  $7\pi$ , which is significantly higher than the threshold of kink instability. Besides, writhing motion is obviously observed by SWAP (Figure 6) and STB/EUVI (Figure 7) during 17:42–17:46 UT. The onset time of writhing is coincident with the commencement of the impulsive phase of the associated flare (Figure 10). Moreover, the kinematic evolution of the CME is divided into two phases using GCS modeling (Figure 19(a)). The CME speeds up from  $\sim 330$  km s $^{-1}$  to  $\sim 1000$  km s $^{-1}$  after the writhing motion. Hence, the prominence eruption is most probably triggered by kink instability.

Using the spectroscopic observations of two tornadoes by the Interface Region Imaging Spectrograph (IRIS; De Pontieu et al., 2014) in Mg II k 2796 Å and Si IV 1393 Å, Yang et al. (2018) found coherent and stable redshifts and blueshifts across the tornado axes lasting for  $\geq 2.5$  hr, which is explained by rotating cool plasmas with temperatures of 0.01–0.1 MK along a relatively stable helical magnetic structure. Panasenco, Martin, and Velli (2014) concluded that the apparent tornado-like prominences result either from counterstreaming and oscillations or from the projection on the plane of the sky of plasma motion instead of a real vortical motion around an axis (Wedemeyer-Böhm et al., 2012). In our study, the eruptive prominence is not a quasi-static tornado at all. The combination of counterclockwise rotation at the leg and the writhing motion during eruption provides clear evidence for untwisting motion of a twisted flux rope as a result of kink instability. The cool plasmas observed in 304 Å are frozen in the field lines, rather than streaming downward along the lines (see Figure 4).

The 3D reconstruction with GCS modeling is successful in tracking the positions and configuration of CMEs, which is very helpful for space weather

prediction. In previous works, the modelings focus on CMEs originating from the frontside observed from Earth (Cheng et al., 2013, 2014b). However, simultaneous observations of CMEs from multiple viewpoints enable us to perform 3D reconstruction of CMEs originating from the farside. In our study, the prominence rises from behind the western limb and undergoes a long slow-rise phase during 13:30–16:30 UT followed by a fast rise. The related flare ribbons and post-flare loops are only visible in the EUV images observed by STA/EUVI, and no enhancements in SXR emissions are detected by GOES. The adoption of  $\phi = 91^\circ$  gives satisfactory fittings (Figures 17 and 18). It should be emphasized that the quiescent filament is very long (Figures 8 and 9), so that the determination of  $\phi$  has an uncertainty (e.g.,  $\sim 1^\circ$ ). In addition, synthetic WL images of the CME are unavailable since the density parameters ( $N_e$ ,  $\sigma_{trailing}$ ,  $\sigma_{leading}$ ) are not taken into account (Thernisien, Howard, and Vourlidas, 2006). In the future, applications of the GCS modeling will be extended by using images of coronagraphs working in WL and UV wavelengths, such as the Metis (Antonucci et al., 2020) and Heliospheric Imager (SoloHI; Howard et al., 2020) on board Solar Orbiter (Müller et al., 2020) and the Lyman-alpha Solar Telescope (LST; Li et al., 2019) on board the Advanced Space-based Solar Observatory (ASO-S; Gan et al., 2019) launched on 9 October 2022.

## 5. Summary

In this paper, we report the multiwavelength observations of an erupting prominence and the associated CME on 13 May 2013. The event occurs behind the western limb in the FOV of SDO/AIA. The main results are summarized as follows:

1. The prominence is supported by a highly twisted magnetic flux rope and shows rapid rotation in the counterclockwise direction during the rising motion. The rotation of the prominence lasts for  $\sim 47$  minutes. The average period, angular speed, and linear speed are  $\sim 806$  s,  $\sim 0.46$  rad min $^{-1}$ , and  $\sim 355$  km s $^{-1}$ , respectively. The total twist angle reaches  $\sim 7\pi$ , which is considerably larger than the threshold for kink instability. Writhing motion during 17:42–17:46 UT is clearly observed by SWAP in 174 Å and STB/EUVI in 304 Å after reaching an apparent height of  $\sim 405$  Mm. Therefore, the prominence eruption is most probably triggered by kink instability. A pair of conjugate flare ribbons and post flare loops are created and observed by STA/EUVI. The onset time of writhing motion is consistent with the commencement of the impulsive phase of the related flare.
2. The 3D morphology and positions of the associated CME are derived using the GCS modeling. The kinetic evolution of the reconstructed CME is divided into a slow-rise phase ( $\sim 330$  km s $^{-1}$ ) and a fast-rise phase ( $\sim 1005$  km s $^{-1}$ ) by the writhing motion. The edge-on angular width of the CME is a constant ( $60^\circ$ ), while the face-on angular width increases from  $96^\circ$  to  $114^\circ$ , indicating a lateral expansion. The latitude of the CME source region decreases slightly from  $\sim 18^\circ$  to  $\sim 13^\circ$ , implying an equatorward deflection during propagation. To the best of our knowledge, this is the first 3D reconstruction of a CME

caused by the eruption of a flux rope due to kink instability. More case studies are required to perform in-depth investigations of their evolutions.

**Acknowledgments** The authors appreciate the referee for valuable and constructive suggestions to improve the quality of this article. We thank Drs. Xiaoli Yan and Zhike Xue in Yunnan Observatories for their helpful discussions. SDO is a mission of NASA’s Living With a Star Program. The AIA data are courtesy of the NASA/SDO science teams. STEREO/SECCHI data are provided by a consortium of the US, UK, Germany, Belgium, and France. This work is supported by the National Key R&D Program of China 2022YFF0503003 (2022YFF0503000), 2021YFA1600500 (2021YFA1600502) and NSFC grants (No. 11790302, 11790300).

## References

- Alexander, D., Liu, R., Gilbert, H.R.: 2006, Hard X-Ray Production in a Failed Filament Eruption. *Astrophys. J.* **653**, 719. DOI. ADS.
- Amari, T., Canou, A., Aly, J.-J., Delyon, F., Alauzet, F.: 2018, Magnetic cage and rope as the key for solar eruptions. *Nature* **554**, 211. DOI. ADS.
- Antiochos, S.K., DeVore, C.R., Klimchuk, J.A.: 1999, A Model for Solar Coronal Mass Ejections. *Astrophys. J.* **510**, 485. DOI. ADS.
- Antonucci, E., Romoli, M., Andretta, V., Fineschi, S., Heinzel, P., Moses, J.D., Naletto, G., Nicolini, G., Spadaro, D., Teriaca, L., Berlicki, A., Capobianco, G., Crescenzo, G., Da Deppo, V., Focardi, M., Frassetto, F., Heerlein, K., Landini, F., Magli, E., Marco Malvezzi, A., Massone, G., Melich, R., Nicolosi, P., Noci, G., Pancrazzi, M., Pelizzo, M.G., Poletto, L., Sasso, C., Schühle, U., Solanki, S.K., Strachan, L., Susino, R., Tondello, G., Uslenghi, M., Woch, J., Abbo, L., Bemporad, A., Casti, M., Dolei, S., Grimani, C., Messerotti, M., Ricci, M., Straus, T., Telloni, D., Zuppella, P., Auchère, F., Bruno, R., Ciaravella, A., Corso, A.J., Alvarez Copano, M., Aznar Cuadrado, R., D’Amicis, R., Enge, R., Gravina, A., Jejić, S., Lamy, P., Lanzafame, A., Meierdierks, T., Papagiannaki, I., Peter, H., Fernandez Rico, G., Giday Sertsu, M., Staub, J., Tsinganos, K., Velli, M., Ventura, R., Verroi, E., Vial, J.-C., Vives, S., Volpicelli, A., Werner, S., Zerr, A., Negri, B., Castronuovo, M., Gabrielli, A., Bertacin, R., Carpentiero, R., Natalucci, S., Marliani, F., Cesa, M., Laget, P., Morea, D., Pieraccini, S., Radaelli, P., Sandri, P., Sarra, P., Cesare, S., Del Forno, F., Massa, E., Montabone, M., Mottini, S., Quattropiani, D., Schillaci, T., Boccardo, R., Brando, R., Pandi, A., Baietto, C., Bertone, R., Alvarez-Herrero, A., García Parejo, P., Cebollero, M., Amoruso, M., Centonze, V.: 2020, Metis: the Solar Orbiter visible light and ultraviolet coronal imager. *Astron. Astrophys.* **642**, A10. DOI. ADS.
- Aulanier, G., Dudík, J.: 2019, Drifting of the line-tied footpoints of CME flux-ropes. *Astron. Astrophys.* **621**, A72. DOI. ADS.
- Awasthi, A.K., Liu, R., Wang, Y.: 2019, Double-decker Filament Configuration Revealed by Mass Motions. *Astrophys. J.* **872**, 109. DOI. ADS.
- Bemporad, A., Mierla, M., Tripathi, D.: 2011, Rotation of an erupting filament observed by the STEREO EUVI and COR1 instruments. *Astron. Astrophys.* **531**, A147. DOI. ADS.
- Berger, T.E., Shine, R.A., Slater, G.L., Tarbell, T.D., Title, A.M., Okamoto, T.J., Ichimoto, K., Katsukawa, Y., Suematsu, Y., Tsuneta, S., Lites, B.W., Shimizu, T.: 2008, Hinode SOT Observations of Solar Quiescent Prominence Dynamics. *Astrophys. J. Lett.* **676**, L89. DOI. ADS.
- Berghmans, D., Hochedez, J.F., Defise, J.M., Lecat, J.H., Nicula, B., Slemzin, V., Lawrence, G., Katsyiannis, A.C., van der Linden, R., Zhukov, A., Clette, F., Rochus, P., Mazy, E., Thibert, T., Nicolosi, P., Pelizzo, M.-G., Schühle, U.: 2006, SWAP onboard PROBA 2, a new EUV imager for solar monitoring. *Advances in Space Research* **38**, 1807. DOI. ADS.
- Brueckner, G.E., Howard, R.A., Koomen, M.J., Korendyke, C.M., Michels, D.J., Moses, J.D., Socker, D.G., Dere, K.P., Lamy, P.L., Llebaria, A., Bout, M.V., Schwenn, R., Simnett, G.M., Bedford, D.K., Eyles, C.J.: 1995, The Large Angle Spectroscopic Coronagraph (LASCO). *Solar Phys.* **162**, 357. DOI. ADS.
- Byrne, J.P., Maloney, S.A., McAteer, R.T.J., Refojo, J.M., Gallagher, P.T.: 2010, Propagation of an Earth-directed coronal mass ejection in three dimensions. *Nature Communications* **1**, 74. DOI. ADS.

- Chae, J., Ahn, K., Lim, E.-K., Choe, G.S., Sakurai, T.: 2008, Persistent Horizontal Flows and Magnetic Support of Vertical Threads in a Quiescent Prominence. *Astrophys. J. Lett.* **689**, L73. DOI. ADS.
- Chen, H.-D., Zhang, J., Ma, S.-L.: 2012, The kinematics of an untwisting solar jet in a polar coronal hole observed by SDO/AIA. *Research in Astronomy and Astrophysics* **12**, 573. DOI. ADS.
- Chen, P.F.: 2011, Coronal Mass Ejections: Models and Their Observational Basis. *Living Reviews in Solar Physics* **8**, 1. DOI. ADS.
- Chen, P.F., Shibata, K.: 2000, An Emerging Flux Trigger Mechanism for Coronal Mass Ejections. *Astrophys. J.* **545**, 524. DOI. ADS.
- Chen, P.-F., Xu, A.-A., Ding, M.-D.: 2020, Some interesting topics provoked by the solar filament research in the past decade. *Research in Astronomy and Astrophysics* **20**, 166. DOI. ADS.
- Chen, Y., Du, G., Zhao, D., Wu, Z., Liu, W., Wang, B., Ruan, G., Feng, S., Song, H.: 2016, Imaging a Magnetic-breakout Solar Eruption. *Astrophys. J. Lett.* **820**, L37. DOI. ADS.
- Cheng, X., Zhang, J., Ding, M.D., Olmedo, O., Sun, X.D., Guo, Y., Liu, Y.: 2013, Investigating Two Successive Flux Rope Eruptions in a Solar Active Region. *Astrophys. J. Lett.* **769**, L25. DOI. ADS.
- Cheng, X., Ding, M.D., Zhang, J., Srivastava, A.K., Guo, Y., Chen, P.F., Sun, J.Q.: 2014a, On the Relationship Between a Hot-channel-like Solar Magnetic Flux Rope and its Embedded Prominence. *Astrophys. J. Lett.* **789**, L35. DOI. ADS.
- Cheng, X., Ding, M.D., Guo, Y., Zhang, J., Vourlidas, A., Liu, Y.D., Olmedo, O., Sun, J.Q., Li, C.: 2014b, Tracking the Evolution of a Coherent Magnetic Flux Rope Continuously from the Inner to the Outer Corona. *Astrophys. J.* **780**, 28. DOI. ADS.
- Cho, K.-S., Lee, J., Bong, S.-C., Kim, Y.-H., Joshi, B., Park, Y.-D.: 2009, A Coronal Mass Ejection and Hard X-Ray Emissions Associated with the Kink Instability. *Astrophys. J.* **703**, 1. DOI. ADS.
- Cremades, H., Bothmer, V.: 2004, On the three-dimensional configuration of coronal mass ejections. *Astron. Astrophys.* **422**, 307. DOI. ADS.
- Cremades, H., Iglesias, F.A., Merenda, L.A.: 2020, Asymmetric expansion of coronal mass ejections in the low corona. *Astron. Astrophys.* **635**, A100. DOI. ADS.
- Curdt, W., Tian, H.: 2011, Spectroscopic evidence for helicity in explosive events. *Astron. Astrophys.* **532**, L9. DOI. ADS.
- De Pontieu, B., Title, A.M., Lemen, J.R., Kushner, G.D., Akin, D.J., Allard, B., Berger, T., Boerner, P., Cheung, M., Chou, C., Drake, J.F., Duncan, D.W., Freeland, S., Heyman, G.F., Hoffman, C., Hurlburt, N.E., Lindgren, R.W., Mathur, D., Rehse, R., Sabolish, D., Seguin, R., Schrijver, C.J., Tarbell, T.D., Wülser, J.-P., Wolfson, C.J., Yanari, C., Mudge, J., Nguyen-Phuc, N., Timmons, R., van Bezooijen, R., Weingrod, I., Brookner, R., Butcher, G., Dougherty, B., Eder, J., Knagenhjelm, V., Larsen, S., Mansir, D., Phan, L., Boyle, P., Cheimets, P.N., DeLuca, E.E., Golub, L., Gates, R., Hertz, E., McKillop, S., Park, S., Perry, T., Podgorski, W.A., Reeves, K., Saar, S., Testa, P., Tian, H., Weber, M., Dunn, C., Eccles, S., Jaeggli, S.A., Kankelborg, C.C., Mashburn, K., Pust, N., Springer, L., Carvalho, R., Kleint, L., Marmie, J., Mazmanian, E., Pereira, T.M.D., Sawyer, S., Strong, J., Worden, S.P., Carlsson, M., Hansteen, V.H., Leenaarts, J., Wiesmann, M., Aloise, J., Chu, K.-C., Bush, R.I., Scherrer, P.H., Brekke, P., Martinez-Sykora, J., Lites, B.W., McIntosh, S.W., Uitenbroek, H., Okamoto, T.J., Gummie, M.A., Auker, G., Jerram, P., Pool, P., Waltham, N.: 2014, The Interface Region Imaging Spectrograph (IRIS). *Solar Phys.* **289**, 2733. DOI. ADS.
- Fan, Y.: 2005, Coronal Mass Ejections as Loss of Confinement of Kinked Magnetic Flux Ropes. *Astrophys. J.* **630**, 543. DOI. ADS.
- Fan, Y., Gibson, S.E.: 2003, The Emergence of a Twisted Magnetic Flux Tube into a Preexisting Coronal Arcade. *Astrophys. J. Lett.* **589**, L105. DOI. ADS.
- Gan, W.-Q., Zhu, C., Deng, Y.-Y., Li, H., Su, Y., Zhang, H.-Y., Chen, B., Zhang, Z., Wu, J., Deng, L., Huang, Y., Yang, J.-F., Cui, J.-J., Chang, J., Wang, C., Wu, J., Yin, Z.-S., Chen, W., Fang, C., Yan, Y.-H., Lin, J., Xiong, W.-M., Chen, B., Bao, H.-C., Cao, C.-X., Bai, Y.-P., Wang, T., Chen, B.-L., Li, X.-Y., Zhang, Y., Feng, L., Su, J.-T., Li, Y., Chen, W., Li, Y.-P., Su, Y.-N., Wu, H.-Y., Gu, M., Huang, L., Tang, X.-J.: 2019, Advanced Space-based Solar Observatory (ASO-S): an overview. *Research in Astronomy and Astrophysics* **19**, 156. DOI. ADS.

- Georgoulis, M.K., Nindos, A., Zhang, H.: 2019, The source and engine of coronal mass ejections. *Philosophical Transactions of the Royal Society of London Series A* **377**, 20180094. DOI. ADS.
- Gilbert, H.R., Alexander, D., Liu, R.: 2007, Filament Kinking and Its Implications for Eruption and Re-formation. *Solar Phys.* **245**, 287. DOI. ADS.
- Gou, T., Veronig, A.M., Liu, R., Zhuang, B., Dumbović, M., Podladchikova, T., Reid, H.A.S., Temmer, M., Dissauer, K., Vršnak, B., Wang, Y.: 2020, Solar Flare-CME Coupling throughout Two Acceleration Phases of a Fast CME. *Astrophys. J. Lett.* **897**, L36. DOI. ADS.
- Green, L.M., Kliem, B., Török, T., van Driel-Gesztelyi, L., Attrill, G.D.R.: 2007, Transient Coronal Sigmoids and Rotating Erupting Flux Ropes. *Solar Phys.* **246**, 365. DOI. ADS.
- Gui, B., Shen, C., Wang, Y., Ye, P., Liu, J., Wang, S., Zhao, X.: 2011, Quantitative Analysis of CME Deflections in the Corona. *Solar Phys.* **271**, 111. DOI. ADS.
- Guo, J.H., Zhou, Y.H., Guo, Y., Ni, Y.W., Karpen, J.T., Chen, P.F.: 2021, Formation and Characteristics of Filament Threads in Double-dipped Magnetic Flux Tubes. *Astrophys. J.* **920**, 131. DOI. ADS.
- Guo, J.H., Ni, Y.W., Zhou, Y.H., Guo, Y., Schmieder, B., Chen, P.F.: 2022, Prominence fine structures in weakly twisted and highly twisted magnetic flux ropes. *Astron. Astrophys.* **667**, A89. DOI. ADS.
- Guo, Y., Ding, M.D., Schmieder, B., Li, H., Török, T., Wiegmann, T.: 2010, Driving Mechanism and Onset Condition of a Confined Eruption. *Astrophys. J. Lett.* **725**, L38. DOI. ADS.
- Hong, J.-C., Jiang, Y.-C., Yang, J.-Y., Zheng, R.-S., Bi, Y., Li, H.-D., Yang, B., Yang, D.: 2013, Twist in a polar blowout jet. *Research in Astronomy and Astrophysics* **13**, 253. DOI. ADS.
- Hood, A.W., Priest, E.R.: 1981, Critical conditions for magnetic instabilities in force-free coronal loops. *Geophysical and Astrophysical Fluid Dynamics* **17**, 297. DOI. ADS.
- Hou, Y.J., Zhang, J., Li, T., Yang, S.H., Li, X.H.: 2018, Eruption of a multi-flux-rope system in solar active region 12673 leading to the two largest flares in Solar Cycle 24. *Astron. Astrophys.* **619**, A100. DOI. ADS.
- Howard, R.A., Michels, D.J., Sheeley, J. N. R., Koomen, M.J.: 1982, The observation of a coronal transient directed at Earth. *Astrophys. J. Lett.* **263**, L101. DOI. ADS.
- Howard, R.A., Moses, J.D., Vourlidas, A., Newmark, J.S., Socker, D.G., Plunkett, S.P., Korendyke, C.M., Cook, J.W., Hurley, A., Davila, J.M., Thompson, W.T., St Cyr, O.C., Mentzell, E., Mehalick, K., Lemen, J.R., Wuelsel, J.P., Duncan, D.W., Tarbell, T.D., Wolfson, C.J., Moore, A., Harrison, R.A., Waltham, N.R., Lang, J., Davis, C.J., Eyles, C.J., Mapson-Menard, H., Simnett, G.M., Halain, J.P., Defise, J.M., Mazy, E., Rochus, P., Mercier, R., Ravet, M.F., Delmotte, F., Auchere, F., Delaboudiniere, J.P., Bothmer, V., Deutsch, W., Wang, D., Rich, N., Cooper, S., Stephens, V., Maahs, G., Baugh, R., McMullin, D., Carter, T.: 2008, Sun Earth Connection Coronal and Heliospheric Investigation (SECCHI). *Space Sci. Rev.* **136**, 67. DOI. ADS.
- Howard, R.A., Vourlidas, A., Colaninno, R.C., Korendyke, C.M., Plunkett, S.P., Carter, M.T., Wang, D., Rich, N., Lynch, S., Thurn, A., Socker, D.G., Thernisien, A.F., Chua, D., Linton, M.G., Koss, S., Tun-Beltran, S., Dennison, H., Stenborg, G., McMullin, D.R., Hunt, T., Baugh, R., Clifford, G., Keller, D., Janesick, J.R., Tower, J., Grygon, M., Farkas, R., Hagood, R., Eisenhauer, K., Uhl, A., Yerushalmi, S., Smith, L., Liewer, P.C., Velli, M.C., Linker, J., Bothmer, V., Rochus, P., Halain, J.-P., Lamy, P.L., Auchère, F., Harrison, R.A., Rouillard, A., Patsourakos, S., St. Cyr, O.C., Gilbert, H., Maldonado, H., Mariano, C., Cerullo, J.: 2020, The Solar Orbiter Heliospheric Imager (SoloHI). *Astron. Astrophys.* **642**, A13. DOI. ADS.
- Ji, H., Wang, H., Schmahl, E.J., Moon, Y.-J., Jiang, Y.: 2003, Observations of the Failed Eruption of a Filament. *Astrophys. J. Lett.* **595**, L135. DOI. ADS.
- Jing, J., Liu, C., Lee, J., Ji, H., Liu, N., Xu, Y., Wang, H.: 2018, Statistical Analysis of Torus and Kink Instabilities in Solar Eruptions. *Astrophys. J.* **864**, 138. DOI. ADS.
- Kaiser, M.L., Kucera, T.A., Davila, J.M., St. Cyr, O.C., Guhathakurta, M., Christian, E.: 2008, The STEREO Mission: An Introduction. *Space Sci. Rev.* **136**, 5. DOI. ADS.
- Kippenhahn, R., Schlüter, A.: 1957, Eine Theorie der solaren Filamente. Mit 7 Textabbildungen. *Zeitschrift für Astrophysik* **43**, 36. ADS.
- Kliem, B., Török, T.: 2006, Torus Instability. *Physical Review Letters* **96**, 255002. DOI. ADS.
- Kliem, B., Titov, V.S., Török, T.: 2004, Formation of current sheets and sigmoidal structure by the kink instability of a magnetic loop. *Astron. Astrophys.* **413**, L23. DOI. ADS.

- Kliem, B., Török, T., Thompson, W.T.: 2012, A Parametric Study of Erupting Flux Rope Rotation. Modeling the “Cartwheel CME” on 9 April 2008. *Solar Phys.* **281**, 137. DOI. ADS.
- Krall, J., St. Cyr, O.C.: 2006, Flux-Rope Coronal Mass Ejection Geometry and Its Relation to Observed Morphology. *Astrophys. J.* **652**, 1740. DOI. ADS.
- Kucera, T.A., Luna, M., Török, T., Muglach, K., Karpen, J.T., Downs, C., Sun, X., Thompson, B.J., Gilbert, H.R.: 2022, Comparison of Two Methods for Deriving the Magnetic Field in a Filament Channel. *Astrophys. J.* **940**, 34. DOI. ADS.
- Kumar, P., Cho, K.-S., Bong, S.-C., Park, S.-H., Kim, Y.H.: 2012, Initiation of Coronal Mass Ejection and Associated Flare Caused by Helical Kink Instability Observed by SDO/AIA. *Astrophys. J.* **746**, 67. DOI. ADS.
- Kuperus, M., Raadu, M.A.: 1974, The Support of Prominences Formed in Neutral Sheets. *Astron. Astrophys.* **31**, 189. ADS.
- Kurokawa, H., Hanaoka, Y., Shibata, K., Uchida, Y.: 1987, Rotating eruption of an untwisting filament triggered by the 3B flare of 25 April, 1984. *Solar Phys.* **108**, 251. DOI. ADS.
- Labrosse, N., Heinzel, P., Vial, J.-C., Kucera, T., Parenti, S., Gunár, S., Schmieder, B., Kilper, G.: 2010, Physics of Solar Prominences: I—Spectral Diagnostics and Non-LTE Modelling. *Space Sci. Rev.* **151**, 243. DOI. ADS.
- Lemen, J.R., Title, A.M., Akin, D.J., Boerner, P.F., Chou, C., Drake, J.F., Duncan, D.W., Edwards, C.G., Friedlaender, F.M., Heyman, G.F., Hurlburt, N.E., Katz, N.L., Kushner, G.D., Levay, M., Lindgren, R.W., Mathur, D.P., McFeaters, E.L., Mitchell, S., Rehse, R.A., Schrijver, C.J., Springer, L.A., Stern, R.A., Tarbell, T.D., Wuelser, J.-P., Wolfson, C.J., Yanari, C., Bookbinder, J.A., Cheimets, P.N., Caldwell, D., Deluca, E.E., Gates, R., Golub, L., Park, S., Podgorski, W.A., Bush, R.I., Scherrer, P.H., Gummin, M.A., Smith, P., Aufer, G., Jerram, P., Pool, P., Souffi, R., Windt, D.L., Beardsley, S., Clapp, M., Lang, J., Waltham, N.: 2012, The Atmospheric Imaging Assembly (AIA) on the Solar Dynamics Observatory (SDO). *Solar Phys.* **275**, 17. DOI. ADS.
- Li, H., Chen, B., Feng, L., Li, Y., Huang, Y., Li, J.-W., Lu, L., Xue, J.-C., Ying, B.-L., Zhao, J., Yang, Y.-T., Gan, W.-Q., Fang, C., Song, K.-F., Wang, H., Guo, Q.-F., He, L.-P., Zhu, B., Zhu, C., Deng, L., Bao, H.-C., Cao, C.-X., Yang, Z.-G.: 2019, The Lyman-alpha Solar Telescope (LST) for the ASO-S mission — I. Scientific objectives and overview. *Research in Astronomy and Astrophysics* **19**, 158. DOI. ADS.
- Li, L., Zhang, J., Peter, H., Priest, E., Chen, H., Guo, L., Chen, F., Mackay, D.: 2016, Magnetic reconnection between a solar filament and nearby coronal loops. *Nature Physics* **12**, 847. DOI. ADS.
- Li, X., Yang, S., Chen, H., Li, T., Zhang, J.: 2015, Trigger of a Blowout Jet in a Solar Coronal Mass Ejection Associated with a Flare. *Astrophys. J. Lett.* **814**, L13. DOI. ADS.
- Lin, J., Forbes, T.G.: 2000, Effects of reconnection on the coronal mass ejection process. *J. Geophys. Res.* **105**, 2375. DOI. ADS.
- Lites, B.W.: 2005, Magnetic Flux Ropes in the Solar Photosphere: The Vector Magnetic Field under Active Region Filaments. *Astrophys. J.* **622**, 1275. DOI. ADS.
- Liu, R., Alexander, D.: 2009, Hard X-ray Emission in Kinking Filaments. *Astrophys. J.* **697**, 999. DOI. ADS.
- Liu, R., Alexander, D., Gilbert, H.R.: 2007, Kink-induced Catastrophe in a Coronal Eruption. *Astrophys. J.* **661**, 1260. DOI. ADS.
- Liu, R., Kliem, B., Török, T., Liu, C., Titov, V.S., Lionello, R., Linker, J.A., Wang, H.: 2012, Slow Rise and Partial Eruption of a Double-decker Filament. I. Observations and Interpretation. *Astrophys. J.* **756**, 59. DOI. ADS.
- Liu, R., Kliem, B., Titov, V.S., Chen, J., Wang, Y., Wang, H., Liu, C., Xu, Y., Wiegmann, T.: 2016, Structure, Stability, and Evolution of Magnetic Flux Ropes from the Perspective of Magnetic Twist. *Astrophys. J.* **818**, 148. DOI. ADS.
- Liu, W., De Pontieu, B., Vial, J.-C., Title, A.M., Carlsson, M., Uitenbroek, H., Okamoto, T.J., Berger, T.E., Antolin, P.: 2015, First High-resolution Spectroscopic Observations of an Erupting Prominence Within a Coronal Mass Ejection by the Interface Region Imaging Spectrograph (IRIS). *Astrophys. J.* **803**, 85. DOI. ADS.
- Liu, Y.A., Liu, Y.D., Hu, H., Wang, R., Zhao, X.: 2018, Multi-spacecraft Observations of the Rotation and Nonradial Motion of a CME Flux Rope Causing an Intense Geomagnetic Storm. *Astrophys. J.* **854**, 126. DOI. ADS.
- Liu, Y., Thernisien, A., Luhmann, J.G., Vourlidas, A., Davies, J.A., Lin, R.P., Bale, S.D.: 2010, Reconstructing Coronal Mass Ejections with Coordinated Imaging and in Situ Observations:



- Global Structure, Kinematics, and Implications for Space Weather Forecasting. *Astrophys. J.* **722**, 1762. DOI. ADS.
- Lörinčík, J., Dudík, J., Aulanier, G., Schmieder, B., Golub, L.: 2021, Imaging Evidence for Solar Wind Outflows Originating from a Coronal Mass Ejection Footpoint. *Astrophys. J.* **906**, 62. DOI. ADS.
- Low, B.C., Hundhausen, J.R.: 1995, Magnetostatic Structures of the Solar Corona. II. The Magnetic Topology of Quiescent Prominences. *Astrophys. J.* **443**, 818. DOI. ADS.
- Luna, M., Karpen, J.T., DeVore, C.R.: 2012, Formation and Evolution of a Multi-threaded Solar Prominence. *Astrophys. J.* **746**, 30. DOI. ADS.
- Luna, M., Moreno-Insertis, F., Priest, E.: 2015, Are Tornado-like Magnetic Structures Able to Support Solar Prominence Plasma? *Astrophys. J. Lett.* **808**, L23. DOI. ADS.
- Mackay, D.H., Karpen, J.T., Ballester, J.L., Schmieder, B., Aulanier, G.: 2010, Physics of Solar Prominences: II—Magnetic Structure and Dynamics. *Space Sci. Rev.* **151**, 333. DOI. ADS.
- Majumdar, S., Patel, R., Pant, V.: 2022, On the Variation in the Volumetric Evolution of CMEs from the Inner to Outer Corona. *Astrophys. J.* **929**, 11. DOI. ADS.
- Majumdar, S., Pant, V., Patel, R., Banerjee, D.: 2020, Connecting 3D Evolution of Coronal Mass Ejections to Their Source Regions. *Astrophys. J.* **899**, 6. DOI. ADS.
- Martin, S.F.: 2003, Signs of helicity in solar prominences and related features. *Advances in Space Research* **32**, 1883. DOI. ADS.
- Michalek, G., Gopalswamy, N., Yashiro, S.: 2003, A New Method for Estimating Widths, Velocities, and Source Location of Halo Coronal Mass Ejections. *Astrophys. J.* **584**, 472. DOI. ADS.
- Mierla, M., Inhester, B., Marqué, C., Rodriguez, L., Gissot, S., Zhukov, A.N., Berghmans, D., Davila, J.: 2009, On 3D Reconstruction of Coronal Mass Ejections: I. Method Description and Application to SECCHI-COR Data. *Solar Phys.* **259**, 123. DOI. ADS.
- Moore, R.L., Sterling, A.C., Hudson, H.S., Lemen, J.R.: 2001, Onset of the Magnetic Explosion in Solar Flares and Coronal Mass Ejections. *Astrophys. J.* **552**, 833. DOI. ADS.
- Moore, R.L., Cirtain, J.W., Sterling, A.C., Falconer, D.A.: 2010, Dichotomy of Solar Coronal Jets: Standard Jets and Blowout Jets. *Astrophys. J.* **720**, 757. DOI. ADS.
- Morosan, D.E., Carley, E.P., Hayes, L.A., Murray, S.A., Zucca, P., Fallows, R.A., McCauley, J., Kilpua, E.K.J., Mann, G., Vocks, C., Gallagher, P.T.: 2019, Multiple regions of shock-accelerated particles during a solar coronal mass ejection. *Nature Astronomy* **3**, 452. DOI. ADS.
- Müller, D., St. Cyr, O.C., Zouganelis, I., Gilbert, H.R., Marsden, R., Nieves-Chinchilla, T., Antonucci, E., Auchère, F., Berghmans, D., Horbury, T.S., Howard, R.A., Krucker, S., Maksimovic, M., Owen, C.J., Rochus, P., Rodriguez-Pacheco, J., Romoli, M., Solanki, S.K., Bruno, R., Carlsson, M., Fludra, A., Harra, L., Hassler, D.M., Livi, S., Louarn, P., Peter, H., Schühle, U., Teriaca, L., del Toro Iniesta, J.C., Wimmer-Schweingruber, R.F., Marsch, E., Velli, M., De Groof, A., Walsh, A., Williams, D.: 2020, The Solar Orbiter mission. Science overview. *Astron. Astrophys.* **642**, A1. DOI. ADS.
- Okamoto, T.J., Liu, W., Tsuneta, S.: 2016, Helical Motions of Fine-structure Prominence Threads Observed by Hinode and IRIS. *Astrophys. J.* **831**, 126. DOI. ADS.
- Panasenco, O., Martin, S.F.: 2008, Topological Analyses of Symmetric Eruptive Prominences. In: Howe, R., Komm, R.W., Balasubramaniam, K.S., Petrie, G.J.D. (eds.) *Subsurface and Atmospheric Influences on Solar Activity, Astronomical Society of the Pacific Conference Series* **383**, 243. ADS.
- Panasenco, O., Martin, S.F., Velli, M.: 2014, Apparent Solar Tornado-Like Prominences. *Solar Phys.* **289**, 603. DOI. ADS.
- Panasenco, O., Martin, S.F., Velli, M., Vourlidas, A.: 2013, Origins of Rolling, Twisting, and Non-radial Propagation of Eruptive Solar Events. *Solar Phys.* **287**, 391. DOI. ADS.
- Panesar, N.K., Tiwari, S.K., Moore, R.L., Sterling, A.C., De Pontieu, B.: 2022, Genesis and Coronal-jet-generating Eruption of a Solar Minifilament Captured by IRIS Slit-raster Spectra. *Astrophys. J.* **939**, 25. DOI. ADS.
- Pant, V., Datta, A., Banerjee, D., Chandrashekhar, K., Ray, S.: 2018, Twisting/Swirling Motions during a Prominence Eruption as Seen from SDO/AIA. *Astrophys. J.* **860**, 80. DOI. ADS.
- Parenti, S.: 2014, Solar Prominences: Observations. *Living Reviews in Solar Physics* **11**, 1. DOI. ADS.

- Patsourakos, S., Vourlidas, A., Stenborg, G.: 2010, The Genesis of an Impulsive Coronal Mass Ejection Observed at Ultra-high Cadence by AIA on SDO. *Astrophys. J. Lett.* **724**, L188. DOI. ADS.
- Pesnell, W.D., Thompson, B.J., Chamberlin, P.C.: 2012, The Solar Dynamics Observatory (SDO). *Solar Phys.* **275**, 3. DOI. ADS.
- Pettit, E.: 1943, The Properties of Solar Prominences as Related to Type. *Astrophys. J.* **98**, 6. DOI. ADS.
- Rust, D.M., Kumar, A.: 1996, Evidence for Helically Kinked Magnetic Flux Ropes in Solar Eruptions. *Astrophys. J. Lett.* **464**, L199. DOI. ADS.
- Rust, D.M., LaBonte, B.J.: 2005, Observational Evidence of the Kink Instability in Solar Filament Eruptions and Sigmoids. *Astrophys. J. Lett.* **622**, L69. DOI. ADS.
- Schmieder, B., Guo, Y., Moreno-Insertis, F., Aulanier, G., Yelles Chaouche, L., Nishizuka, N., Harra, L.K., Thalmann, J.K., Vargas Dominguez, S., Liu, Y.: 2013, Twisting solar coronal jet launched at the boundary of an active region. *Astron. Astrophys.* **559**, A1. DOI. ADS.
- Seaton, D.B., Berghmans, D., Nicula, B., Halain, J.-P., De Groof, A., Thibert, T., Bloomfield, D.S., Raftery, C.L., Gallagher, P.T., Auchère, F., Defise, J.-M., D’Huys, E., Lecat, J.-H., Mazy, E., Rochus, P., Rossi, L., Schühle, U., Slemzin, V., Yalim, M.S., Zender, J.: 2013, The SWAP EUV Imaging Telescope Part I: Instrument Overview and Pre-Flight Testing. *Solar Phys.* **286**, 43. DOI. ADS.
- Shen, C., Wang, Y., Gui, B., Ye, P., Wang, S.: 2011a, Kinematic Evolution of a Slow CME in the Corona Viewed by STEREO-B on 8 October 2007. *Solar Phys.* **269**, 389. DOI. ADS.
- Shen, Y., Liu, Y.: 2012, Evidence for the Wave Nature of an Extreme Ultraviolet Wave Observed by the Atmospheric Imaging Assembly on Board the Solar Dynamics Observatory. *Astrophys. J.* **754**, 7. DOI. ADS.
- Shen, Y., Liu, Y., Su, J., Ibrahim, A.: 2011b, Kinematics and Fine Structure of an Unwinding Polar Jet Observed by the Solar Dynamic Observatory/Atmospheric Imaging Assembly. *Astrophys. J. Lett.* **735**, L43. DOI. ADS.
- Shibata, K., Uchida, Y.: 1986, Sweeping Magnetic Twist Mechanism for the Acceleration of Jets in the Solar Atmosphere. *Solar Phys.* **103**, 299. DOI. ADS.
- Shibata, K., Masuda, S., Shimojo, M., Hara, H., Yokoyama, T., Tsuneta, S., Kosugi, T., Ogawara, Y.: 1995, Hot-Plasma Ejections Associated with Compact-Loop Solar Flares. *Astrophys. J. Lett.* **451**, L83. DOI. ADS.
- Song, H., Li, L., Chen, Y.: 2022, Toward a Unified Explanation for the Three-part Structure of Solar Coronal Mass Ejections. *Astrophys. J.* **933**, 68. DOI. ADS.
- Song, H.Q., Zhou, Z.J., Li, L.P., Cheng, X., Zhang, J., Chen, Y., Chen, C.X., Ma, X.W., Wang, B., Zheng, R.S.: 2018, The Reversal of a Solar Prominence Rotation about Its Ascending Direction during a Failed Eruption. *Astrophys. J. Lett.* **864**, L37. DOI. ADS.
- Srivastava, A.K., Zaqarashvili, T.V., Kumar, P., Khodachenko, M.L.: 2010, Observation of Kink Instability During Small B5.0 Solar Flare on 2007 June 4. *Astrophys. J.* **715**, 292. DOI. ADS.
- Sterling, A.C., Moore, R.L., Falconer, D.A., Adams, M.: 2015, Small-scale filament eruptions as the driver of X-ray jets in solar coronal holes. *Nature* **523**, 437. DOI. ADS.
- Su, Y., van Ballegoijen, A.: 2013, Rotating Motions and Modeling of the Erupting Solar Polar-crown Prominence on 2010 December 6. *Astrophys. J.* **764**, 91. DOI. ADS.
- Su, Y., Wang, T., Veronig, A., Temmer, M., Gan, W.: 2012, Solar Magnetized “Tornadoes:” Relation to Filaments. *Astrophys. J. Lett.* **756**, L41. DOI. ADS.
- Su, Y., Gömöry, P., Veronig, A., Temmer, M., Wang, T., Vanninathan, K., Gan, W., Li, Y.: 2014, Solar Magnetized Tornadoes: Rotational Motion in a Tornado-like Prominence. *Astrophys. J. Lett.* **785**, L2. DOI. ADS.
- Thernisien, A.: 2011, Implementation of the Graduated Cylindrical Shell Model for the Three-dimensional Reconstruction of Coronal Mass Ejections. *Astrophys. J. Suppl. S.* **194**, 33. DOI. ADS.
- Thernisien, A., Vourlidas, A., Howard, R.A.: 2009, Forward Modeling of Coronal Mass Ejections Using STEREO/SECCHI Data. *Solar Phys.* **256**, 111. DOI. ADS.
- Thernisien, A.F.R., Howard, R.A., Vourlidas, A.: 2006, Modeling of Flux Rope Coronal Mass Ejections. *Astrophys. J.* **652**, 763. DOI. ADS.
- Thompson, B.J., Plunkett, S.P., Gurman, J.B., Newmark, J.S., St. Cyr, O.C., Michels, D.J.: 1998, SOHO/EIT observations of an Earth-directed coronal mass ejection on May 12, 1997. *Geophys. Res. Lett.* **25**, 2465. DOI. ADS.
- Thompson, W.T.: 2011, Strong rotation of an erupting quiescent polar crown prominence. *Journal of Atmospheric and Solar-Terrestrial Physics* **73**, 1138. DOI. ADS.

- Thompson, W.T., Kliem, B., Török, T.: 2012, 3D Reconstruction of a Rotating Erupting Prominence. *Solar Phys.* **276**, 241. DOI. ADS.
- Török, T., Kliem, B.: 2003, The evolution of twisting coronal magnetic flux tubes. *Astron. Astrophys.* **406**, 1043. DOI. ADS.
- Török, T., Kliem, B.: 2005, Confined and Ejective Eruptions of Kink-unstable Flux Ropes. *Astrophys. J. Lett.* **630**, L97. DOI. ADS.
- Török, T., Berger, M.A., Kliem, B.: 2010, The writhe of helical structures in the solar corona. *Astron. Astrophys.* **516**, A49. DOI. ADS.
- Török, T., Kliem, B., Titov, V.S.: 2004, Ideal kink instability of a magnetic loop equilibrium. *Astron. Astrophys.* **413**, L27. DOI. ADS.
- Tripathi, D., Reeves, K.K., Gibson, S.E., Srivastava, A., Joshi, N.C.: 2013, SDO/AIA Observations of a Partially Erupting Prominence. *Astrophys. J.* **778**, 142. DOI. ADS.
- Vemareddy, P., Gopalswamy, N., Ravindra, B.: 2017, Prominence Eruption Initiated by Helical Kink Instability of an Embedded Flux Rope. *Astrophys. J.* **850**, 38. DOI. ADS.
- Wang, H., Cao, W., Liu, C., Xu, Y., Liu, R., Zeng, Z., Chae, J., Ji, H.: 2015, Witnessing magnetic twist with high-resolution observation from the 1.6-m New Solar Telescope. *Nature Communications* **6**, 7008. DOI. ADS.
- Wang, J., Yan, X., Guo, Q., Kong, D., Xue, Z., Yang, L., Li, Q.: 2019, Formation and material supply of an active-region filament associated with newly emerging flux. *Mon. Not. Roy. Astron. Soc.* **488**, 3794. DOI. ADS.
- Wang, W., Liu, R., Wang, Y., Hu, Q., Shen, C., Jiang, C., Zhu, C.: 2017, Buildup of a highly twisted magnetic flux rope during a solar eruption. *Nature Communications* **8**, 1330. DOI. ADS.
- Wang, Y., Su, Y., Shen, J., Yang, X., Cao, W., Ji, H.: 2018, High-resolution He I 10830 Å Narrowband Imaging for an M-class Flare. II. Multiple Hot Channels: Their Origin and Destination. *Astrophys. J.* **859**, 148. DOI. ADS.
- Wedemeyer-Böhm, S., Scullion, E., Steiner, O., Rouppe van der Voort, L., de La Cruz Rodriguez, J., Fedun, V., Erdélyi, R.: 2012, Magnetic tornadoes as energy channels into the solar corona. *Nature* **486**, 505. DOI. ADS.
- Williams, D.R., Török, T., Démoulin, P., van Driel-Gesztelyi, L., Kliem, B.: 2005, Eruption of a Kink-unstable Filament in NOAA Active Region 10696. *Astrophys. J. Lett.* **628**, L163. DOI. ADS.
- Wuelser, J.-P., Lemen, J.R., Tarbell, T.D., Wolfson, C.J., Cannon, J.C., Carpenter, B.A., Duncan, D.W., Gradwohl, G.S., Meyer, S.B., Moore, A.S., Navarro, R.L., Pearson, J.D., Rossi, G.R., Springer, L.A., Howard, R.A., Moses, J.D., Newmark, J.S., Delaboudiniere, J.-P., Artzner, G.E., Auchere, F., Bougnet, M., Bouyries, P., Bridou, F., Clotaire, J.-Y., Colas, G., Delmotte, F., Jerome, A., Lamare, M., Mercier, R., Mullet, M., Ravet, M.-F., Song, X., Bothmer, V., Deutsch, W.: 2004, EUVI: the STEREO-SECCHI extreme ultraviolet imager. In: Fineschi, S., Gumm, M.A. (eds.) *Telescopes and Instrumentation for Solar Astrophysics, Society of Photo-Optical Instrumentation Engineers (SPIE) Conference Series* **5171**, 111. DOI. ADS.
- Wyper, P.F., DeVore, C.R., Antiochos, S.K.: 2018, A Breakout Model for Solar Coronal Jets with Filaments. *Astrophys. J.* **852**, 98. DOI. ADS.
- Xia, C., Chen, P.F., Keppens, R., van Marle, A.J.: 2011, Formation of Solar Filaments by Steady and Nonsteady Chromospheric Heating. *Astrophys. J.* **737**, 27. DOI. ADS.
- Xie, H., Ofman, L., Lawrence, G.: 2004, Cone model for halo CMEs: Application to space weather forecasting. *Journal of Geophysical Research (Space Physics)* **109**, A03109. DOI. ADS.
- Xue, X.H., Wang, C.B., Dou, X.K.: 2005, An ice-cream cone model for coronal mass ejections. *Journal of Geophysical Research (Space Physics)* **110**, A08103. DOI. ADS.
- Xue, Z., Yan, X., Cheng, X., Yang, L., Su, Y., Kliem, B., Zhang, J., Liu, Z., Bi, Y., Xiang, Y., Yang, K., Zhao, L.: 2016, Observing the release of twist by magnetic reconnection in a solar filament eruption. *Nature Communications* **7**, 11837. DOI. ADS.
- Xue, Z., Yan, X., Yang, L., Wang, J., Zhao, L.: 2017, Observing Formation of Flux Rope by Tether-cutting Reconnection in the Sun. *Astrophys. J. Lett.* **840**, L23. DOI. ADS.
- Yan, X.L., Xue, Z.K., Liu, J.H., Ma, L., Kong, D.F., Qu, Z.Q., Li, Z.: 2014a, Kink Instability Evidenced by Analyzing the Leg Rotation of a Filament. *Astrophys. J.* **782**, 67. DOI. ADS.
- Yan, X.L., Xue, Z.K., Liu, J.H., Kong, D.F., Xu, C.L.: 2014b, Unwinding Motion of a Twisted Active Region Filament. *Astrophys. J.* **797**, 52. DOI. ADS.

- Yan, X., Li, Q., Chen, G., Xue, Z., Feng, L., Wang, J., Yang, L., Zhang, Y.: 2020, Dynamics Evolution of a Solar Active-region Filament from a Quasi-static State to Eruption: Rolling Motion, Untwisting Motion, Material Transfer, and Chirality. *Astrophys. J.* **904**, 15. DOI. ADS.
- Yang, Z., Tian, H., Peter, H., Su, Y., Samanta, T., Zhang, J., Chen, Y.: 2018, Two Solar Tornadoes Observed with the Interface Region Imaging Spectrograph. *Astrophys. J.* **852**, 79. DOI. ADS.
- Zhang, Q.M.: 2021, A revised cone model and its application to non-radial prominence eruptions. *Astron. Astrophys.* **653**, L2. DOI. ADS.
- Zhang, Q.M.: 2022, Tracking the 3D evolution of a halo coronal mass ejection using the revised cone model. *Astron. Astrophys.* **660**, A144. DOI. ADS.
- Zhang, Q.M., Ji, H.S.: 2014, A swirling flare-related EUV jet. *Astron. Astrophys.* **561**, A134. DOI. ADS.
- Zhang, Q.M., Chen, P.F., Xia, C., Keppens, R.: 2012, Observations and simulations of longitudinal oscillations of an active region prominence. *Astron. Astrophys.* **542**, A52. DOI. ADS.
- Zhang, Q.M., Ning, Z.J., Guo, Y., Zhou, T.H., Cheng, X., Ji, H.S., Feng, L., Wiegmann, T.: 2015, Multiwavelength Observations of a Partially Eruptive Filament on 2011 September 8. *Astrophys. J.* **805**, 4. DOI. ADS.
- Zhang, Q.M., Li, D., Ning, Z.J., Su, Y.N., Ji, H.S., Guo, Y.: 2016, Explosive Chromospheric Evaporation in a Circular-ribbon Flare. *Astrophys. J.* **827**, 27. DOI. ADS.
- Zhang, Q.M., Chen, J.L., Li, S.T., Lu, L., Li, D.: 2022a, Transverse Coronal-Loop Oscillations Induced by the Non-radial Eruption of a Magnetic Flux Rope. *Solar Phys.* **297**, 18. DOI. ADS.
- Zhang, Q., Li, C., Li, D., Qiu, Y., Zhang, Y., Ni, Y.: 2022b, First Detection of Transverse Vertical Oscillation during the Expansion of Coronal Loops. *Astrophys. J. Lett.* **937**, L21. DOI. ADS.
- Zhao, X.P., Plunkett, S.P., Liu, W.: 2002, Determination of geometrical and kinematical properties of halo coronal mass ejections using the cone model. *Journal of Geophysical Research (Space Physics)* **107**, 1223. DOI. ADS.
- Zhou, Y.-H., Chen, P.-F., Zhang, Q.-M., Fang, C.: 2014, Dependence of the length of solar filament threads on the magnetic configuration. *Research in Astronomy and Astrophysics* **14**, 581. DOI. ADS.
- Zou, P., Jiang, C., Wei, F., Zuo, P., Wang, Y.: 2019, A Statistical Study of Solar Filament Eruptions that Form High-speed Coronal Mass Ejections. *Astrophys. J.* **884**, 157. DOI. ADS.